Low-Threshold RNGH Instabilities in Quantum Cascade Lasers

Nikola N. Vuković, Jelena Radovanović, *Member, IEEE*, Vitomir Milanović, and Dmitri L. Boiko

***Abstract*—We show that low-threshold Risken–Nummedal–Graham–Haken (RNGH) instabilities in quantum cascade lasers (QCLs) occur due to a combined effect of the carrier coherence and population grating induced in the gain medium. QCLs with a few mm long cavity exhibit intermittent RNGH self-pulsations while regular self-pulsations are possible in short-cavity QCLs, with the cavity length of 100 μm or smaller. Transient behavior to RNGH self-pulsations in short-cavity QCLs shows features resembling co-operative superradiance which opens a practical way of achieving ultrashort pulse production regimes in the mid-infrared spectral range.**

***Index Terms*—Quantum cascade lasers, laser stability, instabilities and chaos, ultrafast nonlinear optics.**

I. Introduction

The potential of quantum cascade laser (QCL) as a versatile spectroscopic tool could be significantly enhanced if operation in the ultra-short pulse regime would be possible. Such regime would enable time resolved spectroscopic measurements in MIR and FIR ranges for a wide spread of applications such as LIDARs (LIght Detection and Ranging), Earth observation, environmental remote sensing of molecules, in particular, of greenhouse gases, high-speed QCL based communications utilizing the atmospheric transmission windows of 3-5 μm or 8-12 μm and many more [1].

However, ultrafast carrier relaxation at picosecond time scale prohibits passive mode-locking or Q-switching operation in QCLs [2]. Therefore gain switched pulse production has been attempted, yielding 120 ps pulse width [3]. Active mode-locking was achieved in QCLs utilizing diagonal transition, with the upper state lifetime being increased to 50 ps. Yet the diagonal transition renders QCL operation temperature out of the practical use [4].

Manuscript received January 31, 2017; revised April 16, 2017; accepted April 20, 2017. Date of publication May 3, 2017; date of current version July 3, 2017. This work was supported in part by Swiss National Science Foundation project FastIQ, ref. no. IZ73Z0_152761, in part by the Ministry of Education, Science and Technological Development (Republic of Serbia), ref. no. III 45010, COST ACTIONs BM1205, MP1204 and MP1406, in part by the European Union's Horizon 2020 research and innovation programme (SUPERTWIN, ref. no. 686731), and in part by the Canton of Neuchâtel. *(Corresponding author: Nikola N. Vukovic.)*

N. N. Vukovic, J. Radovanovic, and V. Milanovic are with the School of Electrical Engineering, University of Belgrade 11120, Belgrade Serbia (e-mail: nikolavukovic89@gmail.com; radovanovic@etf.bg.ac.rs; milanovic@etf.bg.ac.rs).

D. L. Boiko is with the Centre Suisse d'Électronique et de Microtechnique (CSEM) CH-2002, Neuchâtel Switzerland (e-mail: dmitri.boiko@csem.ch).

Color versions of one or more of the figures in this paper are available online at http://ieeexplore.ieee.org.

Digital Object Identifier 10.1109/JSTQE.2017.2699139

One more promising approach to generate short MIR pulses has emerged from experimental observations of low-threshold [5] Risken-Nummedal-Graham-Haken (RNGH) multimode instabilities in QCLs [6], [7]. However, the second-order interferometric autocorrelation measurements have shown that the output optical pulses have significant stochastic constituent [4], if these autocorrelation traces should not be attributed at all to coherence spikes.

In general, the multimode RNGH instabilities are related to a non-adiabatic [8] behavior of the medium polarization, excitation of rapid coupled oscillations of the medium polarization P and population inversion N. They show up as self-pulsations in the output laser emission, whereas the optical spectrum is expected to be split in two mode clusters (sidebands) with frequency separation of the order of the Rabi oscillation frequency.

Below the RNGH instability threshold, the optical mode is fully controlled by the laser cavity. The buildup of Rabi oscillations at above the multimode instability threshold indicates that now a macroscopic medium polarization has the major impact on the optical field in the laser cavity. The original RNGH theory, which was established for a CW operating *unidirectional ring laser*, requires the pump rates of at least 9 times above the lasing threshold.

However in [5], a clear Rabi frequency splitting between two clusters of lasing modes was observed in QCLs operating at just slightly above the lasing threshold, indicating multimode RNGH instability in these *Fabry-Pérot (FP) cavity lasers*. In some cases, e.g., at high pump rates, a continuous spectrum of modes extending over the twice the Rabi frequency range can emerge. Interestingly, the RNGH instability was observed as in ridge waveguide QCLs as in buried heterostructure QCLs. Although the role of spatial hole burning (SHB) in lowering the RNGH instability threshold was understood, it was thought [9] that the low-threshold RNGH instability does not occur just as a result of the induced grating of carrier population. Therefore, an additional assumption was made in [9] on a *built-in saturable absorber* in the cavity of QCL, allowing for a reduction of the RNGH threshold from 9-fold excess to about 1.1 times above the lasing threshold. As a matter of fact, the saturable absorber has been known to lower the instability threshold [10]. However, the nature of saturable absorption in QCLs has never been fully clarified [1]. In particular, the authors in [9] have evoked the Kerr lensing effect as a possible mechanism responsible for the saturable absorption. In case of narrow ridge waveguide lasers, due to overlap of the waveguide mode tails and the metal contact deposited on the waveguide, the Kerr lensing may lead to saturable

absorption. However it cannot produce the saturable absorption effect of the same strength in buried heterostructure QCLs. At the same time low-threshold RNGH instability was observed in both ridge waveguide and buried heterostructure QCLs.

An alternative approach to explain the unusually low RNGH instability threshold in QCLs was proposed in [11]. The idea stems from a parametric gain picture yielding instability of the main cavity mode, along the line of comb generation in optically pumped dielectric micro-disk resonators with third-order $\chi^{(3)}$ non-linearity. Mid-IR intersubband transitions in semiconductor QWs do produce strong third-order nonlinearity [12], [13]. However optically passive microdisk resonators have special cavity design in order to reach parametric instability threshold. In particular they employ whispering gallery modes with very small transverse size, very high quality factor ($Q \sim 10^8$) and operate with circulating pump power in the resonator on the order of several hundreds of watts [14]. Electrically pumped Mid-IR QCLs with FP cavities cannot reproduce such environment and reach parametric instability caused by material third-order nonlinearity $\chi^{(3)}$.

The origin of instability in [11] was attributed to parametric gain for an offset frequency wavelets co-propagating in the gain medium which is subjected to saturation by the main lasing mode. Essentially this consideration is based on a lumped gain rate equation model for a laser in which spatial hole burning is introduced in a phenomenological way. Apart from a lumped gain picture, this approach is conceptually identical to the original one by Risken and Nummedal who consider propagation of perturbation wavelets in the traveling wave picture. The results reported in [11] agrees with experimental observations however phenomenologically introduced spatial hole burning effect masks certain important points of the analysis and hence it leaves space for further study of the subject.

In this paper, we develop another alternative model for low-threshold multimode RNGH instability in a QCL *without saturable absorber and providing a strict consideration of the saturation and spatial modulation effects in the traveling wave picture*. This is a more realistic representation for a monolithic single-section *FP cavity laser* as compare to the one in [6], [7], [9]. The main difference from all other models cited above consists in (i) accounting for the induced carrier coherence grating alongside with the carrier population grating and in (ii) accounting for the carrier diffusion process that leads to relaxation of both gratings. In contrast to the lumped gain in [11], we utilize travelling wave picture and we clarify the role of carrier coherence grating. The outcomes of our analysis for the RNGH instability threshold in QCLs are in perfect agreement with the numerical simulations based on a travelling wave (TW) rate equation model as well as with the experimental data available in the literature [5], [9], [15]. Interestingly, we find that regular self-pulsations at picosecond time scale are possible in short-cavity QCLs.

II. Model Description

A. QCL as a Model System for RNGH Instabilities

As a model system for RNGH instability, we consider an InGaAs QCL with a direct transition, having the carrier lifetime (longitudinal relaxation time) T_1 of about one picosecond. This is much smaller than the cavity round-trip time. We do not examine any particular case of heterostructure epilayers or lateral cavity design since in the experiments with ridge waveguide [9] or buried heterostructure QCLs [5], these have no or little impact on the RNGH instability. The parameters of our QCL model system are summarized in Table I. In the table, the optical mode confinement factor and transparency carrier density for QCL are defined using the overall thickness of epilayers in the period. The photon lifetime in the cavity exceeds the dephasing time (transverse relaxation time) T_2, so as the dynamic behavior reported here is intrinsically different from the Class-D laser dynamics discussed in [16].

TABLE I
Dynamic Model Parameters for InGaAs QCLs in this Paper

Symbol	Quantity	Value [17]
λ	Lasing wavelength	10 μm
T_1	Carrier lifetime	1.3 ps
T_2	Carrier dephasing time	140 fs
T_{2_eff}	Effective carrier dephasing time in the presence of diffusion	138 fs
T_g	Relaxation time of the carrier population grating	0.927 ps
T_{2_g}	Relaxation time of the coherence grating	128 fs
α_i	Intrinsic material loss	24 cm^{-1}
D	Diffusion coefficient	180 cm^2/s
n_g	Group refractive index	3.3
R_1, R_2	Cavity facet reflection coefficients	27%
Γ	Optical mode confinement factor	0.5
$\partial g/\partial n$	Differential material gain	2.1×10^{-4} cm^3/s
n_t	Transparency carrier density	7×10^{14} cm^{-3}

B. Coupled-Mode Rate Equation Model

As a starting point of our analysis we use semiclassical Maxwell-Bloch (MB) equations for a two-level system. Following along the lines of the approach from [18] and accounting for the diffusion term in the Schrödinger equation [19], we obtain the following system of rate equations:

$$\dot{\rho}_{ab} = i\omega\rho_{ab} + i\frac{\mu E}{\hbar}\Delta - \frac{\rho_{ab}}{T_2} + D\frac{\partial^2\rho_{ab}}{\partial z^2} \tag{1}$$

$$\dot{\Delta} = -2i\frac{\mu E}{\hbar}(\rho^*_{ab} - \rho_{ab}) + \frac{\Delta_{pump} - \Delta}{T_1} + D\frac{\partial^2\Delta}{\partial z^2} \tag{2}$$

$$\partial_z^2 E - \frac{n_g^2}{c^2}\partial_t^2 E = \Gamma\frac{N\mu}{\varepsilon_0 c^2}\partial_t^2(\rho^*_{ab} + \rho_{ab}) + \frac{n_g l'_0}{c}\partial_t E \tag{3}$$

The difference between our MB equations for QCLs and equations used in [9] is the coherence diffusion term $D\partial^2\rho_{ab}/\partial z^2$ that appears in the first equation. Here $\rho_{ab} = \rho^*_{ba}$ is the off-diagonal element of the density matrix, the non-equilibrium carrier density $N\Delta = N(\rho_{bb} - \rho_{aa})$ is represented as the population inversion between the upper (index "*bb*") and lower (index "*aa*") levels of the lasing transition, $N\mu(\rho^*_{ab} + \rho_{ab})$ is the active medium polarization ("coherence"), ω and μ denote the resonant frequency and the dipole matrix element of the lasing transition, respectively, $N\Delta_{pump}/T_1$ is the pump rate due to injection of electrons into the upper lasing level, N is defined by the doping density in the injector region and D is the diffusion coefficient for electrons in the plane of active QWs of the QCL

structure. E, Γ and n_g stand for the cavity mode electric field, the overlap between the optical mode and the active region and the group refractive index for the cavity mode, respectively. Note that the differential material gain is $\partial g/\partial n = \omega T_2 \mu^2/\hbar n_g^2 \varepsilon_0$ (n is carrier density) and l_0' is the linear loss coefficient.

Numerical simulations with the travelling wave rate equation model reported below were accomplished by introducing in (1)–(3) two slowly varying amplitudes for the counter propagating waves in the FP cavity and distinguishing the medium's polarizations associated with the forward and backward traveling waves [20].

C. Approximation of Coupled-Mode Rate Equation Model

In [21], a comprehensive approach for analysis of multimode instabilities in a ring laser was established using a truncated set of coupled-mode equations. A similar approach was applied in [9] for the case of FP-cavity QCLs. However it does not take into account the spatial harmonics of induced macroscopic polarization of the gain medium in the *FP-cavity laser* or *bidirectional ring laser*. As a result, in the limit of adiabatic elimination of the medium polarization, it does not agree with well-established models for a Class-B laser dynamics [22]. (See discussion to (7)–(11) below and also Appendix A and Section III-E. We stress that by no means our considerations for bidirectional ring lasers and FP cavity lasers can be applied to the unidirectional ring laser considered in [6], [7]). In order to match the experimentally measured RNGH threshold of $\sim$1.1 I_{th} (I_{th} is the lasing threshold pump current), the model in [9] assumes that there is a built-in saturable absorber [10] in the monolithic cavity of QCL, which has never been unambiguously confirmed [1].

In order to elucidate another possible origin of the low-threshold RNGH instability, we have expanded the MB equations (1)–(3) into a truncated set of self-consistent coupled mode equations. Our analysis of the SHB effect has shown that as soon as the spatial grating of carrier population is taken into account (the terms $\Delta_2^{\pm}$ below), the third-order spatial harmonics of the induced macroscopic polarization grating (the terms η_{++} and η_{--} below) have to be accounted for in the expansion:

$$E(z,t) = \frac{1}{2}\left[E_+^* e^{-i(\omega t - kz)} + E_+ e^{i(\omega t - kz)}\right] + \frac{1}{2}\left[E_-^* e^{-i(\omega t + kz)} + E_- e^{i(\omega t + kz)}\right] \quad (4)$$

$$\rho_{ab}(z,t) = \left(\eta_+ + \eta_{++} e^{-2ikz}\right) e^{i(\omega t - kz)} + \left(\eta_- + \eta_{--} e^{2ikz}\right) e^{i(\omega t + kz)} \quad (5)$$

$$\Delta(z,t) = \Delta_0 + \Delta_2^+ e^{2ikz} + \Delta_2^- e^{-2ikz} \quad (6)$$

where $E(z,t)$ and $\Delta(z,t)$ are real-valued variables ($\Delta_2^{+^*} = \Delta_2^-$) and the amplitudes $E_\pm$, $\eta_\pm$, $\eta_{\pm\pm}$, Δ_0 and $\Delta_2^\pm$ vary slowly in time and space as compared to the plane wave carriers. The two optical carrier waves propagating at frequency ω and wavenumbers $\pm k$ stand for the initial lasing mode in the cavity.

Substitution of (4)–(6) in MBE (1)–(3) leads to the following coupled-mode equations in the slowly varying envelope approximation:

$$\frac{n_g}{c}\partial_t E_\pm = \mp \partial_z E_\pm - i\frac{N\mu\Gamma\omega}{c n_g \varepsilon_0}\eta_\pm - \frac{1}{2} l_0 E_\pm \quad (7)$$

$$\partial_t \eta_\pm = \frac{i\mu}{2\hbar}\left(\Delta_0 E_\pm + \Delta_2^\mp E_\mp\right) - \frac{\eta_\pm}{T_2} - k^2 D \eta_\pm \quad (8)$$

$$\partial_t \eta_{\pm\pm} = \frac{i\mu}{2\hbar} E_\pm \Delta_2^\mp - \frac{\eta_{\pm\pm}}{T_2} - 9Dk^2\eta_{\pm\pm} \quad (9)$$

$$\partial_t \Delta_0 = \frac{\Delta_{pump} - \Delta_0}{T_1} + \frac{i\mu}{\hbar}\left(E_+^*\eta_+ + E_-^*\eta_- - c.c\right) \quad (10)$$

$$\partial_t \Delta_2^\pm = \frac{i\mu}{\hbar}\left(E_\pm^*\eta_\mp - E_\mp\eta_\pm^* - E_\pm\eta_{\pm\pm}^* + E_\mp^*\eta_{\mp\mp}\right) - \frac{\Delta_2^\pm}{T_1} - 4k^2 D\Delta_2^\pm \quad (11)$$

where l_0 is the cavity loss coefficient that comprises intrinsic material losses and output coupling losses. In order to verify our coupled-mode expansion (4)–(6), we have performed the adiabatic-following approximation test [8] (see Appendix A) and find that the adiabatic approximation for our set of equations is in excellent agreement with the well-established Class-B laser model.

Next, we carry out a linear stability analysis of our model system (7)–(11). In what follows we introduce the effective relaxation times that account for the contribution from the diffusion terms $T_g = (T_1^{-1} + 4Dk^2)^{-1}$, $T_{2\_g} = (T_2^{-1} + 9Dk^2)^{-1}$,$T_{2\_\mathrm{eff}} = (T_2^{-1} + Dk^2)^{-1}$ (These relaxation times are quoted in Table I). We also define new variables $e_\pm = l_0 E_\pm \mu/\hbar$, $\pi_\pm = \eta_\pm l_0/(\Delta_{th} T_{2\_\mathrm{eff}})$, $n_0 = \Delta_0 l_0/(\Delta_{th} T_{2\_\mathrm{eff}})$ and $n_\pm = \Delta_\pm l_0/(\Delta_{th} T_{2\_\mathrm{eff}})$. The pump rate is accounted for by the parameter $p = \Delta_{pump}/\Delta_{th}$, which measures the pump rate excess above the lasing threshold in the absence of SHB, and $N\Delta_{th} = c\hbar\varepsilon_0 n_g l_0/\Gamma\omega T_{2\_\mathrm{eff}}\mu^2$ is the carrier density at the lasing threshold.

We obtain the steady-state solution of (7)–(11) assuming an arbitrary initial phase θ of the wave propagating in the positive z axis direction (forward wave). Because the optical mode field $E(z,t)$ and the population parameter $\Delta(z,t)$ in (4)–(6) are the real-valued variables, the phase of the wave propagating in the backward direction is –θ, yielding the following solution for CW lasing regime:

$$e_\pm = e^{\pm i\theta} l_0 \mathcal{E}, n_0 = \frac{\nu_0 l_0}{T_{2\_\mathrm{eff}}}, n_\pm = \frac{-e^{\mp i2\theta} l_0(\nu_0 - 1)}{T_{2\_\mathrm{eff}}}$$

$$\pi_\pm = \frac{i}{2} e^{\pm i\theta} l_0 \mathcal{E}, \pi_{\pm\pm} = -\frac{T_{2\_g}}{T_{2\_\mathrm{eff}}}\frac{i}{2}(\nu_0 - 1)e^{\pm i3\theta} l_0 \mathcal{E}$$

$$\mathcal{E} = \sqrt{\frac{p - \nu_0}{2T_1 T_{2\_\mathrm{eff}}}} \quad (12)$$

is the normalized field amplitude. Note that variables $n_-^* = n_+$, $e_-^* = e_+$ are complex conjugate while the variables $\pi_-^* = -\pi_+$, $\pi_{--}^* = -\pi_{++}$ are anti-conjugate.

The SHB increases the effective lasing threshold and reduces the slope efficiency. To account for this effect, we introduce an additional parameter $\nu_0 = \Delta_0/\Delta_{th}$, which is the ratio of the

$$\nu_0 = \frac{1}{2}\left(p+1+\frac{T_{2\_\mathrm{eff}}}{T_{2\_g}}+\frac{2T_1T_{2\_\mathrm{eff}}}{T_gT_{2\_g}}\right)-\sqrt{\frac{1}{4}\left(p+1+\frac{T_{2\_\mathrm{eff}}}{T_{2\_g}}+\frac{2T_1T_{2\_\mathrm{eff}}}{T_gT_{2\_g}}\right)^2-p\left(1+\frac{T_{2\_\mathrm{eff}}}{T_{2\_g}}\right)-\frac{2T_1T_{2\_\mathrm{eff}}}{T_gT_{2\_g}}} \tag{13}$$

fundamental harmonic of the average carrier density $N\Delta_0$ to its value at the lasing threshold $N\Delta_{th}$ (at $p = 1$), when SHB effect does not yet settle–in; see (13), shown at the top of the page.

At lasing threshold, $\nu_0 = 1$ and it increases above the threshold (at $p > 1$). At very high pump rate ($p >> 1$), ν_0 asymptotically approaches the value of $1 + T_{2\_\mathrm{eff}}/T_{2\_g}$.

D. Linear Stability Matrix

The linear stability analysis of the steady-state solution (12)–(13), is performed by introducing small perturbations $\delta e_\pm = \delta e_r \pm i\delta e_i$, $\delta\pi_\pm = \pm\delta\pi_r + i\delta\pi_i$, $\delta\pi_{\pm\pm} = \mp\delta\pi_{rr} - i\delta\pi_{ii}$, δn_0 and $\delta n_\pm = \delta n_r \pm i\delta n_i$ in the corresponding variables of the coupled-mode equations (7)–(11). Taking into account the complex conjugate and anti-conjugate relationships between the variables $\delta n_- = \delta n_+^*$, $\delta e_- = \delta e_+^*$, $\delta\pi_- = -\delta\pi_+^*$, $\delta\pi_{--} = -\delta\pi_{++}^*$, we obtain the linearized system of differential equations in (14), shown at the bottom of the page, where $\tau = n_g/cl_0$ is the photon lifetime in the cavity.

Using the ansatz from [7], we recast all perturbations δX to the main lasing mode in the form of propagating wavelets $\delta X \propto \exp(in_g\Omega z/c + \Lambda t)$ and obtain a 9×9 eigenproblem with respect to Lyapunov exponent Λ. Here $\Omega n_g/c$ is the detuning of the propagation constant from the one of the lasing mode and $-\mathrm{Im}(\Lambda)$ is the frequency offset. For all practical situations of interest in this study, the approximation $\mathrm{Im}(\Lambda) \approx -\Omega$ suffices. Note that only that solutions of (14) with the positive increment $\mathrm{Re}(\Lambda) > 0$ will build-up in the cavity after several round-trips, which fulfill the cavity round-trip phase self-repetition condition $2\Omega L n_g/c = 2\pi n$, where L is the cavity length and n is an integer number.

Via a transformation of variables, the 9×9 matrix in (14) can always be altered into a block-diagonal form with 5×5 and 4×4 blocks. For example in the case of initial phase $\theta = 0$, such transformation is straightforward, yielding us the eigenproblem (15), shown at the bottom of the next page.

Out of these two matrices, only the smaller size 4×4 matrix may exhibit Lyapunov exponent with the positive real part in the practically feasible range of pump currents (see Fig. 1(a)) and thus may lead to unstable CW lasing regime observed in experiment [5], [9]. The 5×5 block shows only stable solutions in a large range of pump rates above the lasing threshold. Thus for a QCL from Table I, this behavior is observed up to p $\sim$ 50 times above the lasing threshold (Fig. 1(a), solid curves). The initial phase θ has no impact on the instability increment $\mathrm{Re}(\Lambda)$ and occurrence of the instability itself. However the required transformation and hence the set of variables responsible for instability are both changing with the initial phase of the mode θ. Therefore, it is not possible to identify the nature of instability (RNGH-like or of a different kind) from the set of variables involved.

At the same time we find that whatever the initial phase θ, the offset frequency $\Omega_{\max}$ at the maximum increment $\mathrm{Re}(\Lambda)$ in

$$\frac{d}{dt}\begin{bmatrix}\delta\pi_i\\ \delta e_r\\ \delta n_0\\ \delta n_r\\ \delta\pi_{ii}\\ \delta\pi_r\\ \delta e_i\\ \delta n_i\\ \delta\pi_{rr}\end{bmatrix} = \begin{bmatrix}
-\frac{1}{T_{2_\mathrm{eff}}} & \frac{\nu_0-(\nu_0-1)\cos 2\theta}{2T_{2_\mathrm{eff}}} & \frac{\mathcal{E}\cos\theta}{2} & \frac{\mathcal{E}\cos\theta}{2} & 0 & 0 & -\frac{(\nu_0-1)\sin 2\theta}{2T_{2_\mathrm{eff}}} & -\frac{\mathcal{E}\sin\theta}{2} & 0\\
\frac{1}{\tau} & -\frac{1}{2\tau}-i\Omega & 0 & 0 & 0 & 0 & 0 & 0 & 0\\
-4\mathcal{E}\cos\theta & -2\mathcal{E}\cos\theta & -\frac{1}{T_1} & 0 & 0 & 4\mathcal{E}\sin\theta & -2\mathcal{E}\sin\theta & 0 & 0\\
-2\mathcal{E}\cos\theta & \left[(\nu_0-1)\frac{T_{2_g}}{T_{2_\mathrm{eff}}}\cos 3\theta-\cos\theta\right]\mathcal{E} & 0 & -\frac{1}{T_g} & 2\mathcal{E}\cos\theta & -2\mathcal{E}\sin\theta & \left[(\nu_0-1)\frac{T_{2_g}}{T_{2_\mathrm{eff}}}\sin 3\theta+\sin\theta\right]\mathcal{E} & 0 & -2\mathcal{E}\sin\theta\\
0 & \frac{(\nu_0-1)\cos 2\theta}{2T_{2_\mathrm{eff}}} & 0 & -\frac{\mathcal{E}\cos\theta}{2} & -\frac{1}{T_{2_g}} & 0 & -\frac{(\nu_0-1)\sin 2\theta}{2T_{2_\mathrm{eff}}} & -\frac{\mathcal{E}\sin\theta}{2} & 0\\
0 & \frac{(\nu_0-1)\sin 2\theta}{2T_{2_\mathrm{eff}}} & -\frac{\mathcal{E}\sin\theta}{2} & \frac{\mathcal{E}\sin\theta}{2} & 0 & -\frac{1}{T_{2_\mathrm{eff}}} & -\frac{\nu_0+(\nu_0-1)\cos 2\theta}{2T_{2_\mathrm{eff}}} & \frac{\mathcal{E}\cos\theta}{2} & 0\\
0 & 0 & 0 & 0 & 0 & -\frac{1}{\tau} & -\frac{1}{2\tau}-i\Omega & 0 & 0\\
2\mathcal{E}\sin\theta & \left[-(\nu_0-1)\frac{T_{2_g}}{T_{2_\mathrm{eff}}}\sin 3\theta+\sin\theta\right]\mathcal{E} & 0 & 0 & 2\mathcal{E}\sin\theta & -2\mathcal{E}\cos\theta & \left[(\nu_0-1)\frac{T_{2_g}}{T_{2_\mathrm{eff}}}\cos 3\theta+\cos\theta\right]\mathcal{E} & -\frac{1}{T_g} & 2\mathcal{E}\cos\theta\\
0 & -\frac{(\nu_0-1)\sin 2\theta}{2T_{2_\mathrm{eff}}} & 0 & \frac{\mathcal{E}\sin\theta}{2} & 0 & 0 & -\frac{(\nu_0-1)\cos 2\theta}{2T_{2_\mathrm{eff}}} & -\frac{\mathcal{E}\cos\theta}{2} & -\frac{1}{T_{2_g}}
\end{bmatrix} \cdot \begin{bmatrix}\delta\pi_i\\ \delta e_r\\ \delta n_0\\ \delta n_r\\ \delta\pi_{ii}\\ \delta\pi_r\\ \delta e_i\\ \delta n_i\\ \delta\pi_{rr}\end{bmatrix} \tag{14}$$

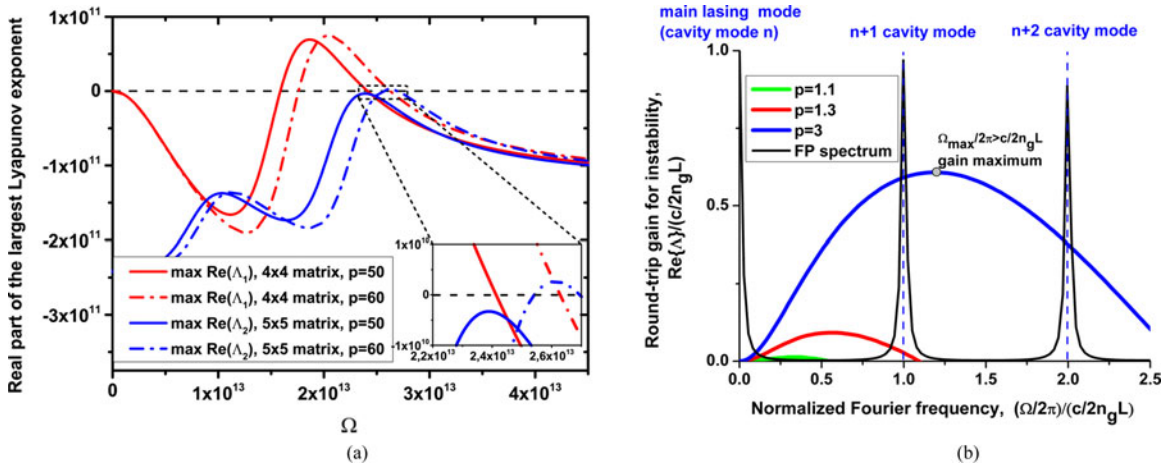

Fig. 1. (a) Spectra of instability increments (largest real parts of the Lyapunov exponents) of the 4 × 4 (red curves) and 5 × 5 matrix (blue curves) blocks at p = 50 (solid) and p = 60 (dash-dotted lines). (b) Positive offset frequency part of the spectrum of the round-trip gain for instability in a 100 μm long QCL at normalized pump rate of p = 1.1 (green curve), p = 1.3 (red curve) and p = 3. The black curve indicates the Airy function of the cold cavity (not in scale). QCL parameters are taken from Table I.

4 × 4 matrix is close to the Rabi oscillation frequency $\Omega_{Rabi} = \sqrt{(p-\nu_0)/T_1 T_{2\_\mathrm{eff}}}$ (see Section III below). This allows us to attribute this instability to the RNGH-like behavior discussed in [6], [7] (See also Appendix B).

This behavior should be contrasted with the one reported in [9], where the carrier coherence grating (9) has not been taken into account. If one omits the variables $\delta\pi_{rr}$ and $\delta\pi_{ii}$ associated with the carrier coherence grating, the smaller size 4 × 4 matrix block in (15) simply becomes of 3 × 3 size. It still exhibits an instability at small pump rate above the lasing threshold [9], however, at significantly lower frequencies around $\Omega_{SHB} = \sqrt{T_1^{-1}\sqrt{(p-1)/3T_1T_2}} \sim \sqrt{\Omega_{Rabi}/T_1}/\sqrt[4]{3}$. Therefore this instability has been mistakenly attributed in [9] to the SHB effect (further discussion can be found in Sections III-B and III-E).

The larger size 5 × 5 matrix block in (15), which shows only stable solutions in the presence of the carrier coherence grating (9) and at reasonable pump rates, takes the form of a 4 × 4 matrix after dropping out $\delta\pi_{rr}$ and $\delta\pi_{ii}$ variables. Our numerical analysis shows that it may lead to RNGH instability at the pump rate approximately 10 times above the lasing threshold, in agreement with the theoretical predictions from [6], [7]. The RNGH instability threshold always remains that high unless a saturable absorber is introduced to the model system [10], the possibility which was studied in [9].

We thus argue that inclusion of both grating terms (9) and (11) allows one to obtain low-threshold RNGH instability in a *FP cavity laser* (or *bidirectional ring laser*) without saturable absorber. This RNGH instability is of different origin from the one discussed in [9]: In our case it originates from the smaller size 4 × 4 matrix block in (15) and not from the 5 × 5 block. Furthermore, the coherence grating (9), the inclusion of which was validated in the adiabatic-following approximation test (Appendix A), renders the RNGH threshold associated with the 5 × 5 block further more prohibitively higher (at p ∼ 60 instead of the initial value of p ∼ 9-10 in the original RNGH instability case for a *unidirectional ring laser* without SHB), see Fig. 1(a). Note that it is impossible to make similar parallels with the

$$\det\begin{bmatrix} -\frac{1}{T_{2\_\mathrm{eff}}}-\Lambda & \frac{1}{2T_{2\_\mathrm{eff}}} & \frac{\mathcal{E}}{2} & \frac{\mathcal{E}}{2} & 0 \\ \frac{1}{\tau} & -\frac{1}{2\tau}-i\Omega-\Lambda & 0 & 0 & 0 \\ -4\mathcal{E} & -2\mathcal{E} & -\frac{1}{T_1}-\Lambda & 0 & 0 \\ -2\mathcal{E} & \left[(\nu_0-1)\frac{T_{2\_g}}{T_{2\_\mathrm{eff}}}-1\right]\mathcal{E} & 0 & -\frac{1}{T_g}-\Lambda & 2\mathcal{E} \\ 0 & \frac{(\nu_0-1)}{2T_{2\_\mathrm{eff}}} & 0 & -\frac{\mathcal{E}}{2} & -\frac{1}{T_{2\_g}}-\Lambda \end{bmatrix} = 0,$$

$$\det\begin{bmatrix} -\frac{1}{T_{2\_\mathrm{eff}}}-\Lambda & -\frac{(2\nu_0-1)}{2T_{2\_\mathrm{eff}}} & \frac{\mathcal{E}}{2} & 0 \\ -\frac{1}{\tau} & -\frac{1}{2\tau}-i\Omega-\Lambda & 0 & 0 \\ -2\mathcal{E} & \left[(\nu_0-1)\frac{T_{2\_g}}{T_{2\_\mathrm{eff}}}+1\right]\mathcal{E} & -\frac{1}{T_g}-\Lambda & 2\mathcal{E} \\ 0 & -\frac{(\nu_0-1)}{2T_{2\_\mathrm{eff}}} & -\frac{\mathcal{E}}{2} & -\frac{1}{T_{2\_g}}-\Lambda \end{bmatrix} = 0 \quad (15)$$

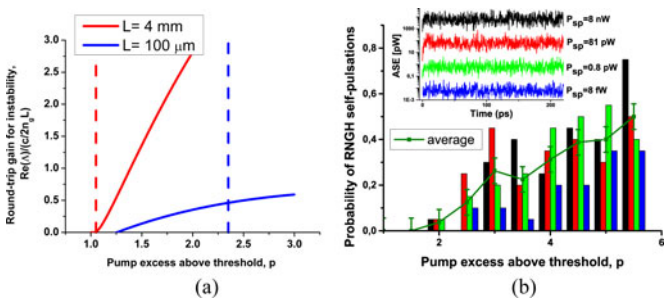

Fig. 2. (a) Lyapunov stability analysis: round-trip gain for instability in the nearest-neighbor modes vs. pump excess above threshold for the QCLs with the cavity lengths of 4 mm (red curve) and 100 μm (blue curve). In long-cavity QCL, the RNGH threshold (16) is very low, at $p_{th2} = 1.05$ (red dashed line), while $p_{th2} = 2.35$ in the short-cavity QCL (blue dashed line). (b) Probability of occurrence of RNGH self-pulsations in QCL with 100 μm long cavity is plotted as a function of the pump excess above lasing threshold p for different levels of spontaneous polarization noise used in the numerical simulations (bar colors) as well as the average probability over all 80 realizations (curve). The inset shows amplified spontaneous emission (ASE) power for corresponding levels of spontaneous polarization noise (curve colors) when QCL is below the lasing threshold ($p = 0.9$). QCL parameters are given in Table I.

treatment from [11] because it utilizes the laser rate equation model in the lumped gain picture.

III. Results and Discussion

A. RNGH Instability Threshold

For QCLs that have the cavity length of 2-4 mm, our linear stability matrix (15) predicts the multimode RNGH instability at a pump rate of a few percent above the lasing threshold. This prediction is in agreement with numerous experimental data available in the literature [5], [9], [16]. Our numerical simulations based on TW rate equation model also confirm this behavior and the transition to multimode operation at just above the lasing threshold (see Section III-B).

At the same time in the case of a short-cavity single-section QCL of just 100 μm long, the linear stability analysis based on (15) shows that the real part of the Lyapunov exponent Re(Λ) becomes positive at the pump rate p just slightly above 1 (Fig 1(b)). However, in this case our TW numerical simulations reveal stable CW operation regime up to the pump rate of 2-2.5 times above the lasing threshold (see Fig. 2(b)). We examine this contradiction in further details and arrive to a new insight about the RNGH threshold condition, which we introduce below.

Fig. 1(b) illustrates the spectral behavior of the increment $\mathrm{Re}(\Lambda)$. Only positive offset frequencies are shown, because $\mathrm{Re}(\Lambda)$ is an even function of Ω. The zero offset frequency corresponds to the initially lasing mode. The instability increment is normalized to the cavity mode separation, so as Fig. 1(b) shows the spectral shape of the round-trip gain coefficient $2\mathrm{Re}(\Lambda)\mathrm{n_g L/c}$ for various (non-lasing) cavity modes. In the figure, the instability gain spectra are depicted at three different pump rates of $p = 1.1$, 1.3 and 3 (green, red and blue curves, respectively). We also indicate the locations of a few cavity modes by plotting the Airy function of the "cold cavity" (black curve, not in scale).

The original RNGH condition [6], [7] for multimode instability in a CW operating single-mode laser just requires a positive instability increment at a frequency of another cavity mode. An example that matches this definition is the instability gain curve plotted in Fig. 1(b) for p = 1.3 (red curve). It shows that the gain coefficient is positive for the first two adjacent (non-lasing) cavity modes at $\Omega/2\pi = \pm c/2n_g L$. In Fig. 2(a), this gain coefficient is plotted as a function of the pump rate (solid blue curve). According to the conventional definition [6], [7], the multimode instability should occur at p = 1.25, when the instability gain becomes positive at some of the non-lasing cavity modes. However not every small-amplitude instability necessarily develops into large-amplitude RNGH self-pulsations. In fact there are many other possibilities such as mode jumps or slow phase instabilities [23]–[25]. Further details can be found in [26].

In order to verify the RNGH threshold condition, we perform a series of numerical simulations based on the travelling wave rate equation model. Our model is adapted from [20] by removing saturable absorber section. It utilizes slowly varying envelope approximation for the field amplitude, which is a real valued variable in the model. It cannot reproduce mode jumps, while the amplitude instabilities can be detected by examining the simulated waveforms. The model incorporates Langevin force terms that seed spontaneous polarization noise into the system (these terms are not indicated in (1)–(3), but an example can be found in [20]). In Fig. 2(b) we vary the power of the noise injected into the system over 6 orders of magnitude, from eight to two orders below the polarization noise level in homogeneously broadened ensemble of two-level quantum oscillators (see also [26] and reference therein]). The inset in Fig. 2(b) indicates the corresponding output power of amplified spontaneous emission P_{sp}. For each set of parameters $(p,\ P_{\mathrm{sp}})$ we perform a series of 20 simulations and statistically count the occurrence rate (probability) of the RNGH like self-pulsations (see an example in Sect. III.C). Fig. 2(b) shows no systematic correlations between the occurrence of RNGH instability and spontaneous noise power P_{sp} injected into the system. We have not seen the impact of the noise power on the lasing regime. Only the delay time to the onset of emission was changing. The noise power that we will use in all the simulations throughout the rest of the manuscript is $P_{\mathrm{sp}} = 81$ pW (red trace in Fig. 2(b)). In Fig. 2(b) we also plot the average probability at a given p over all 80 realizations (solid curve) with the dispersion of ± 0.056 (error bars).

The data in Fig. 2(b) attests that there is no multimode RNGH self-pulsations at the pump rate p = 1.5. This is in contradiction with the conventional definition of the RNGH instability threshold, foreseeing $p_{th2} = 1.25$ (Fig. 2(a), blue curve). At $p = 2$, only a few realizations have resulted in RNGH self-pulsations with the average probability of 0.04 being below the uncertainty limit. The RNGH self-pulsations confidently develop at p between 2 and 2.5, with $p = 2.5$ being the first point in Fig. 2(b) for which the occurrence probability exceeds the uncertainty range.

Obviously, the results of our numerical simulations do not agree with the multimode instability condition proposed by Risken and Nummedal [6], and Graham and Haken [7].

Analyzing the data in Fig. 2(b), we notice that RNGH self-pulsations confidently occur when the instability gain maxima at $\Omega_{\max} \approx \pm\Omega_{Rabi}$ is on resonance with the nearest-neighbor modes at $\pm c\pi/n_g L$ or at a higher frequency offset as in the case indicated by the blue curve in Fig. 1(b). The threshold for RNGH self-pulsations corresponding to this refinement is indicated in Fig. 2(a) by a vertical dashed line $p_{\rm th2} = 2.35$, which is in reasonable agreement with the numerical results in Fig. 2(b).

The proposed refinement for the RNGH self-pulsations threshold has a clear physical meaning. Recall that RNGH instability in a CW single-mode laser arises due to Rabi splitting of the lasing transition induced by the lasing mode. As a result of such spectral broadening and reshaping of the gain curve, the laser can provide sufficient initial optical gain to other longitudinal modes at the early stage of instability [27]. Most importantly, this shall lead to large-amplitude self-pulsations at a later stage such that the medium polarization does not simply follow adiabatically the optical field but instead it becomes a leading variable of this dynamical system [7]. Therefore we assume that the initial perturbation to the lasing mode has a pulse shape and we apply the pulse area theorem for non-adiabatic pulse propagation [8], [28]. In the most general case, the characteristic time of such perturbation pulse is roughly a half of the cavity round-trip time $\tau_p \sim Ln_g/c$. From the pulse area theorem, the optical pulse is unstable and the pulse area grows if, initially, $\Omega_{Rabi} \cdot \tau_p > \pi$. Because the maximum gain for RNGH instability is located at the offset frequency $\Omega_{\max} \approx \pm\Omega_{Rabi}$ (see Section III-B), we conclude that the multimode RNGH instability occurs only when:

$$|\Omega_{\max}|/2\pi \geq c/2Ln_g \tag{16}$$

The blue curve in Fig. 1(b) satisfies this condition. Otherwise, the pulse area of the initial perturbation decreases without reaching non-adiabatic behavior of the medium polarization. This case is indicated by the red curve in Fig. 1(b).

The condition (16) raises considerably the RNGH self-pulsations threshold in short-cavity devices because of the large frequency separation between the cavity modes (Fig. 2(a) blue curve and vertical line). However, it has minor impact in QCLs with long cavities (Fig. 2(a) red curve and vertical line). In [26] we have obtained the analytic expression for the pump rate at RNGH self-pulsations threshold (16).

B. RNGH Self-Pulsations in a QCL With Long Cavity

We utilize a single-section QCL with the cavity length of 4 mm as a model system for long-cavity devices. The linear stability analysis indicates the self-pulsations threshold (16) of $p_{th2} = 1.05$. For the pump rate $p = 1.2$, which is slightly above the instability threshold, we do observe a quasi-periodic chaotic behavior in the output power waveform [Figs. 3(a)]. Here the cavity round-trip time is 88 ps, much larger than the carrier lifetime T_1 (Table I). Fig. 3(a) shows the first ten and the last ten cavity round-trips from the entire simulation domain which extends over 100 cavity round-trips. The laser is initially not pumped and the pump current is switched on at a time t = 0 s. The onset of the lasing emission is seen in less than 3 cavity round-trips (at t $\sim$ 200 ps, Fig. 3(a)). Comparing the self-pulsations in the first and last 10 round-trips in Fig. 3(a), one can see that after additional 3 cavity round-trips, the system reaches a steady regime of quasi-periodic (chaotic) self-pulsations, in good agreement with the inverse value of the gain coefficient in Fig. 2(a) (red curve, yielding 1/0.38 = 2.6 round-trips). In the inset of Fig. 3(a) we trace the evolution of the medium polarization *P* versus carrier density *N*. Both *P* and *N* values are taken in the vicinity of the laser facet and are normalized at transparency carrier density. The P-N attractor has a characteristic butterfly shape typical for a chaotic behavior in a Lorenz-type system [29]. In total, QCL reaches the steady regime of chaotic self-pulsations just in 6 cavity round-trips ($\sim$530 ps). This time appears too short for establishing fixed phase relationships between many individual modes as in the case of actively mode-locked (ML) QCLs with built-in electroabsorber sections [30], [31]. However the waveform in Fig. 3(a) clearly attests that our single-section QCL does not operate in ML regime. Indeed the peak to background ratio of interferometric autocorrelation (AC) trace in Fig. 3(b) is worse than 8:3 while for a ML regime it should be close to 8:1 [32]. Thus, our quasi-periodic chaotic pulse train from Fig. 3 perfectly explains the experimentally measured interferometric AC traces in [9], including nontrivial pulse structure in between cavity round-trips. The background-free intensity AC in Fig. 3(b) has the contrast of 2:1.75. This corresponds to the literature case of "noisy CW signal" [32]. Appearance of correlation peaks at cavity round-trips is due to the quasi-periodic nature of the waveform. In relation to this example of non-regular pulse train we recall that observation of regular frequency comb in the optical spectrum does not indicate that the modes have fixed phase relationships and the laser produces a regular pulse train. With increasing pump rate, the optical field waveform develops into a quasi-periodic square wave. An example of the temporal behavior of the optical field amplitude, medium polarization and carrier density is depicted in Fig. 4. The optical field behavior [Fig. 4(a), black curve, left axis] appears to be quite similar to the one predicted in [21], Lugiato et al., for a long-cavity unidirectional ring laser at high pump rates. However in our case, the average field amplitude is zero due to quenching of the initially CW lasing mode and emergence of the two symmetric sidebands in the optical spectrum. Like the optical field, the medium polarization shows the square-wave behavior. However, its waveform pattern is not identical to that one of the optical field [Fig. 4(a), red curve, right axis]. This is not surprising if one takes into account the scattering of counter-propagating waves on the induced gratings of carrier coherence and population. Most importantly, the medium polarization does not follow the optical field adiabatically. Instead, the medium polarization itself defines the optical field dynamics.

One can see in Figs. 4(a) that the pattern of the square wave almost repeats itself after each round-trip in the cavity (88 ps), indicating that a wave packet with complex envelope travels back and forth in the cavity. Its envelope just slightly changes at each round-trip, yielding the quasi-periodic chaotic behavior. A different pattern is seen in the waveforms of the optical power and carrier population [Fig. 4(b), left and right axis respectively]. These variables are either quadratic with respect

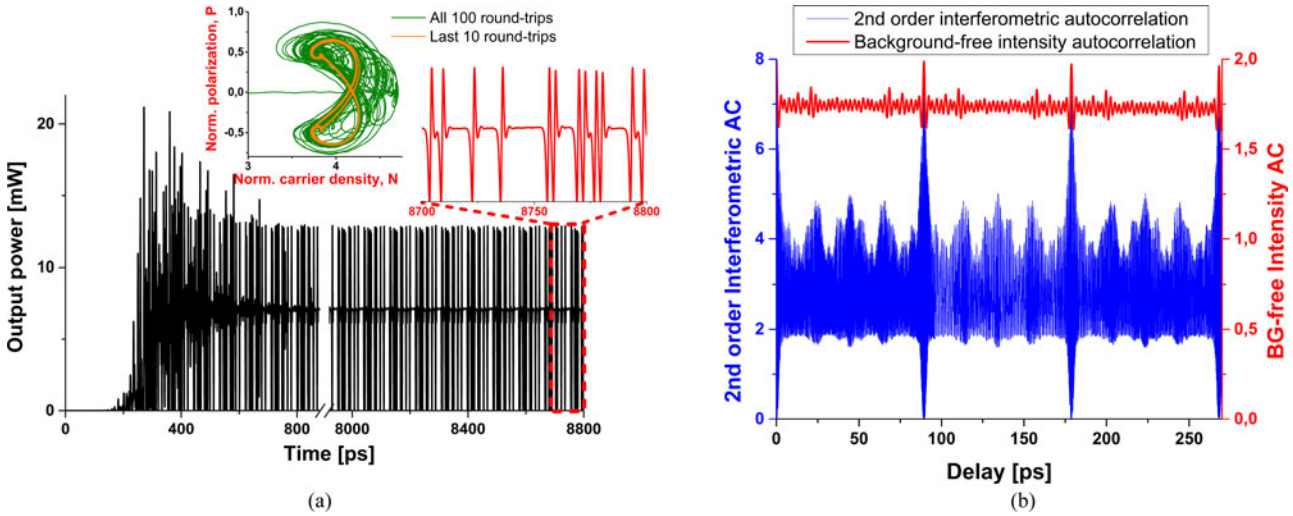

Fig. 3. Results of numerical simulations with TW model for 4 mm long QCL (cavity round-trip time is 88 ps): Panel (a) depicts the output power waveform for the first ten and the last ten (out of 100) round-trips in the cavity with zoom on the last round-trip. The inset shows chaotic P-N attractor. The behavior during all 100 cavity round-trips is depicted with the green curve, while the orange curve signifies the last 10 round-trips, when the system reaches the steady regime of quasi-periodic (chaotic) self-pulsations. (b) Second-order interferometric AC (blue curve, left axis) and background free intensity AC trace (red curve, right axis). The QCL is pumped at p = 1.2 times above the lasing threshold. Other parameters are shown in Table I.

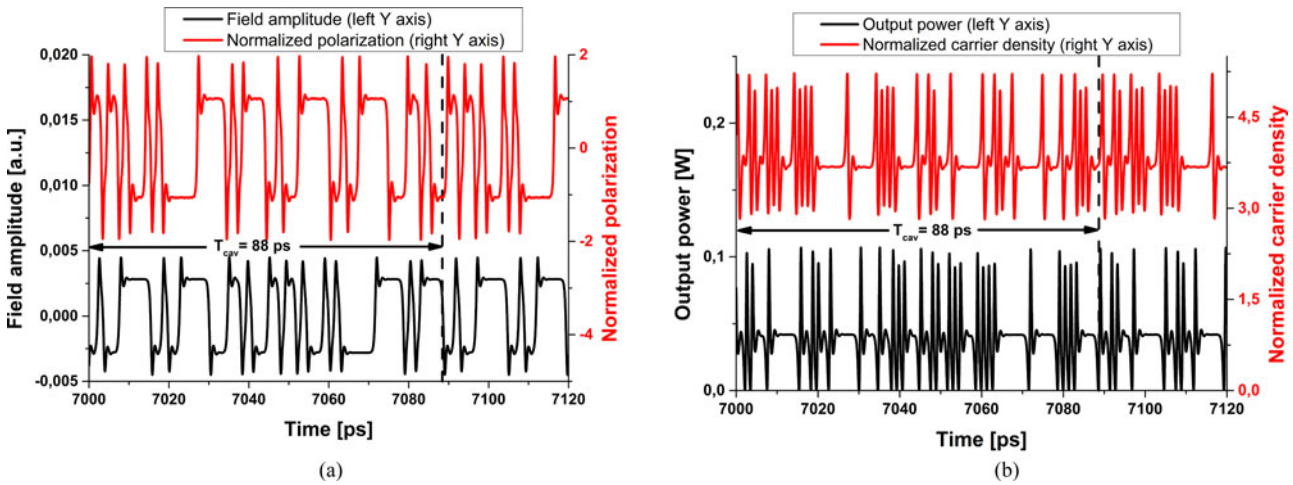

Fig. 4. Results of numerical simulations with TW model for QCL with the cavity length of 4 mm: The optical field waveform and normalized medium polarization for the wave propagating in the positive z axis direction (a), output power and normalized carrier density (b). All values are taken nearby the output facet of the laser cavity. The QCL model parameters are the same as in Fig. 3 but the pump rate is of $p = 2.2$.

to the optical field or have a contribution from the product of the optical field amplitude and the medium polarization [see (7)–(11)]. Each waveform in Fig. 4(b) exhibits spikes that are superimposed on a steady level. The spikes are caused by intermittent behavior of the optical field and polarization, while the steady-state component attests for the symmetry of the field and polarization square wave patterns. The period of spikes is roughly a half of that for polarization waveform, yielding the Lorenz-type attractor as shown in the inset of Fig. 3(a).

All these features seen in the time-domain waveforms are directly imprinted into the optical, radio frequency (RF) spectra, spectra of carriers and polarization (Fig. 5). Due to the standing wave pattern of the optical field and induced carrier coherence and carrier population gratings, there are several Rabi oscillation modes in the cavity. In order to extract their frequencies, we have made an additional small-signal analysis of (7)–(11) but this time, we keep fixed the amplitude of the optical wave. We find that Rabi oscillations are possible at the main frequency Ω_{Rabi} as well as at the two other frequencies $(1 + 2^{-1/2})^{1/2}\Omega_{Rabi}$ and $(1 - 2^{-1/2})^{1/2}\Omega_{Rabi}$, where:

$$\Omega_{Rabi} = \sqrt{\frac{p - \nu_0(p)}{T_1 T_{2\_\mathrm{eff}}}} \tag{17}$$

Out of these three Rabi oscillations modes, only the main one (17) is associated with the gain medium variables in the 4 $\times$ 4 matrix block of (15) responsible for RNGH instability in our FP-cavity laser. In Fig. 5(a) we also compare the extracted spectra with the evolution of the peak gain frequency $\Omega_{\max}$ for multimode RNGH instability (see Fig. 1(b)) as well as with the possible frequency of multimode instability due SHB effect,

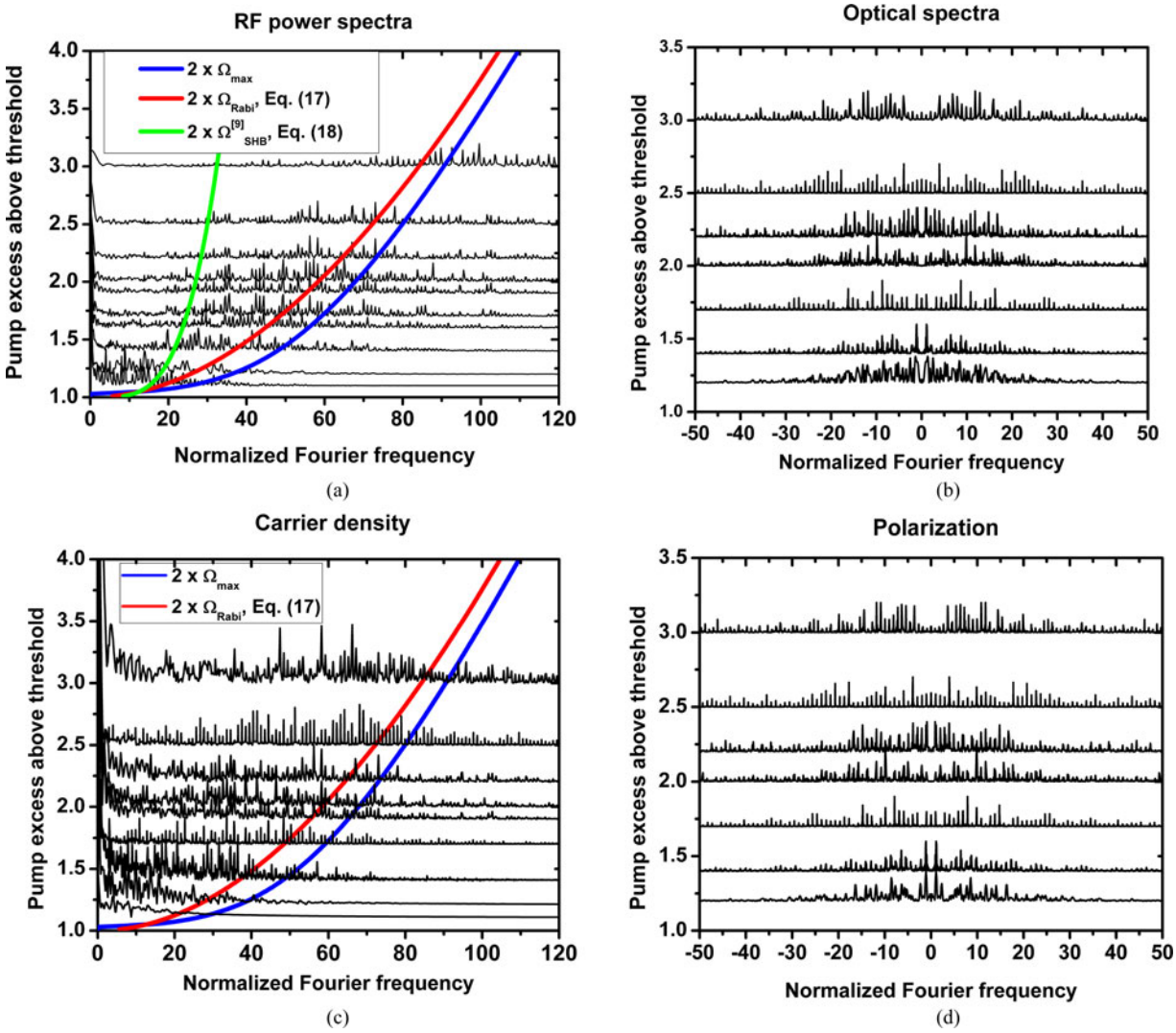

Fig. 5. Results of numerical simulations with TW model for QCL with the cavity length of 4 mm: Evolution of QCL (a) RF power spectrum, (b) optical spectrum, (c) carrier density and (d) polarization when pumped above the lasing threshold. In (a) and (c) red and blue curves indicate expected location of modulation sidebands originating from Ω_{Rabi} and $\Omega_{\max}$. The green curve shows that one for $\Omega^{[9]}_{SHB}$. The frequency is normalized to longitudinal mode spacing of 11.4 GHz. The model parameters are the same as in Fig. 3. Fig 5.(a) is reproduced from [33] with permission of Springer.

which is predicted in [9] to be well below Ω_{Rabi} and $\Omega_{\max}$:

$$\Omega^{[9]}_{SHB} = \sqrt{\frac{1}{T_1}\sqrt{\frac{p-1}{3T_1T_2}}} \tag{18}$$

Note that all these frequencies ($\Omega_{\rm Rabi}$,$\Omega_{\max}$ and $\Omega^{[9]}_{\rm SHB}$) are obtained using a small-signal approach. Because the optical power is $\propto E^2$ while the carrier dynamics is governed by terms $\propto EP$, in Fig. 5(a) we plot these frequencies scaled by a factor of 2. Note that the peak gain frequency $\Omega_{\max}$ is quite close to the Rabi oscillation frequency (compare the red and blue curves in Fig. 5(a)). The evolution of the RF power spectrum in Fig. 5(a) almost follows along the curves for 2 $\Omega_{\rm Rabi}$ and 2 $\Omega_{\max}$ frequencies, exhibiting the spectral broadening and the frequency shift of the modulation band that increases with the pump rate. Note however that it is unrealistically to expect the exact matching between the numerical simulations for large-amplitude self-pulsations and the outcomes of the small-signal analysis in (16)–(18). At the same time the spectral broadening and the frequency shift in Fig. 5(a) are clearly much larger than for a possible multimode instability at the frequency $\Omega^{[9]}_{\rm SHB}$ due to SHB effect [9] (green curve). Therefore we attribute the spectral behavior in Fig. 5(a) to RNGH-like instability (see also Section III-E). Since the output power waveform (as in Fig. 4(b)) can be regarded as a series of ultrafast spikes superimposed on a steady intensity level, the modulation band seen in the RF power spectrum at the frequency 2 $\Omega_{\rm Rabi}$ is primarily due to the spiking behavior of the output power. The optical spectra are displayed in Fig. 5(b). The initially lasing mode at $\Omega = 0$ (the carrier wave) is quenched and the spectra reveal two symmetric sidebands. Since the RF modulation spectra of the output power exhibit modulation bands at the frequency 2 $\Omega_{\rm Rabi}$ [see Fig. 5(a)] one would expect to observe the modulation sidebands at frequencies $\pm\Omega_{\rm Rabi}$ in the optical spectra as well. However

these considerations do not take into account large phase hops due to intermittent behavior of the optical field (compare the intensity waveform in the inset of Fig. 3(a) and the field amplitude in Fig. 4(a)). Obviously, the phase of the optical field does not contribute to the RF power spectrum. At the same time, the large phase hops of $\pm\pi$ impact directly the overall optical spectrum, warping its envelope as compare to the envelope of the RF power spectrum. From the waveform in Fig. 4(a) one can see that the average repetition frequency of such phase hops is much lower than the spectral band of each spike in Fig. 4(b). As a result, the spectral envelope of modulation sidebands in the optical spectrum is shifted to lower frequency. The experimental data available in the literature also attest that RNGH instability does not always lead to observation of a clear Rabi splitting in the optical mode spectrum of a QCL (see Appendix B). In Fig. 5(c) we plot the frequency-domain representation of the carrier density dynamics at different values of p. The spectra shows broadening and modulation of the carrier density at frequencies up to twice the Rabi oscillation frequency. This behavior is similar to the evolution of RF spectra in Fig. 5(a). However the modulation band nearby 2 Ω_{Rabi} is less pronounced and the spectra exhibit almost all frequency components down to $\Omega = 0$. This behavior can be attributed to a slow response of the carrier density and carrier population grating to the rapid variations $\propto EP$ in (10)–(11). The cutoff frequencies are of $1/2\pi T_1 = 122$ GHz and $1/2\pi T_g = 172$ GHz for the average density and population grating, respectively. The medium polarization waveform in the frequency domain representation is displayed in Figs. 5(d). As expected, it shows very good resemblance with the optical spectra in Fig. 5(b).

C. RNGH Instability in a QCL With Short Cavity

We now move on to the case of short-cavity QCLs and consider an example of QCL with the cavity length L = 100 μm, for which the linear stability analysis predicts the RNGH threshold (16) of $p_{\mathrm{th2}} = 2.35$ (see Fig. 2(a), blue vertical line). At pump rate above the instability threshold, e.g., at p = 2.5 as in Fig. 6, the first emission burst of high peak power is followed by steady regime of regular self-pulsations [Fig. 6(a)]. The FWHM pulsewidth of the first emission burst is of 0.5ps while for regular self-pulsations it is of 0.6 ps width. The system attractor plotted in the P-N plane indicates that the laser transits to regular self-pulsations (or even self-oscillations) just after a few roundtrips in the cavity [inset of Fig.6(a) shows intensity self-pulsations]. The period of regular self-pulsations (field variable) is close to the cavity round-trip time of 2.2 ps with the optical field amplitude (and the medium polarization) changing sign at each half period. This can be seen from the 8-like shape of P-N attractor in inset of Fig. 6(a). This behavior attests that this is not a usual mode-locking regime. In Fig. 6(b) the contrast ratio of the *interferometric* AC is 8:1.5 (blue curve, left axis) and the one for background-free intensity AC (red curve, right axis) is of 2:0.6. Although the process is coherent, the IAC does not reach the peak-to background ratio of 8:1 (2:0) because intensity pulse width is close to the period of intensity self-pulsations.

Figs. 6(c) and (d) show the optical and RF power spectra respectfully, when the pump rate p is in the range of 2.2 to 3.9 times above the lasing threshold. In case of short-cavity QCL operating at just above the instability threshold, only two main frequency components are excited in the optical spectrum [Fig. 6(c)]. With increasing pump rate, the spectrum remains symmetric with respect to initially lasing mode and the two main spectral components are located at the two nearest-neighbor modes. The multimode RNGH instability occurs when the frequency Ω_{max} of the maximum gain for instability is on resonance with the first adjacent cavity mode [Fig. 6(c), blue curve]. However, with increasing pump rate, the frequency of self-pulsations does not follow the increasing frequency Ω_{max} or Rabi oscillation frequency (red curve). Higher order modes start to appear in the optical spectrum as opposed to continuous frequency rise. We attribute this behavior to the cavity round-trip self-repetition condition (see Sect. III.B). With the increase of normalized pump p the waveform is still periodic but it changes from regular sine-like shape to some more irregular one since more spectral components are included with the increase of pump p. Eventually it will become square wave for p $\sim$ 5 (values that are not of practical importance).

Note that the frequency of self-pulsations is slightly lower than the cold cavity mode spacing due to the group velocity reduction. It can be attributed to propagation phenomenon of a high-energy pulse in resonant medium, the process which can be regarded as continual absorption of energy from the pulse leading edge and re-emission of energy into the pulse trailing edge [28].

A quite similar behavior is reported in [21] for a short-cavity unidirectional ring laser. However in case of the ring laser, the optical field does not change the sign at each half-period. As a consequence, the main lasing mode at $\Omega = 0$ is not quenched. One can trace a few other similarities between multimode instability in QCLs discussed here and the RNGH instability in unidirectional ring lasers from [21]. In particular, one very important question has been challenged but has not been answered in [21]. More specifically, the mechanism, which is responsible for regular self-pulsations in case of short-cavity laser and chaotic pulsations in the long-cavity case, has not been elucidated. This qualitative change in dynamic behavior becomes even more wondering if one considers the affinity between the 8-shape attractor in case of regular self-pulsations in Fig. 6(a) and the butterfly-shape attractor in case of chaotic self-pulsations in Fig. 3(a).

D. Comment on Coherence Length

The *P* and *N* variables used here are introduced following the approach of [20]. In particular, the variable *P* measures the order parameter in the system (the carrier density in the coherent state) and has the same units as the carrier density *N*. In Figs. 3 and 6, both variables *P* and *N* are normalized on the transparency carrier density.

In Fig. 6 the order parameter *P* is high. It reaches about a half of the value for *N* that precedes the emission pulse. This feature is observed as in the first emission burst [inset in Fig. 6(a),

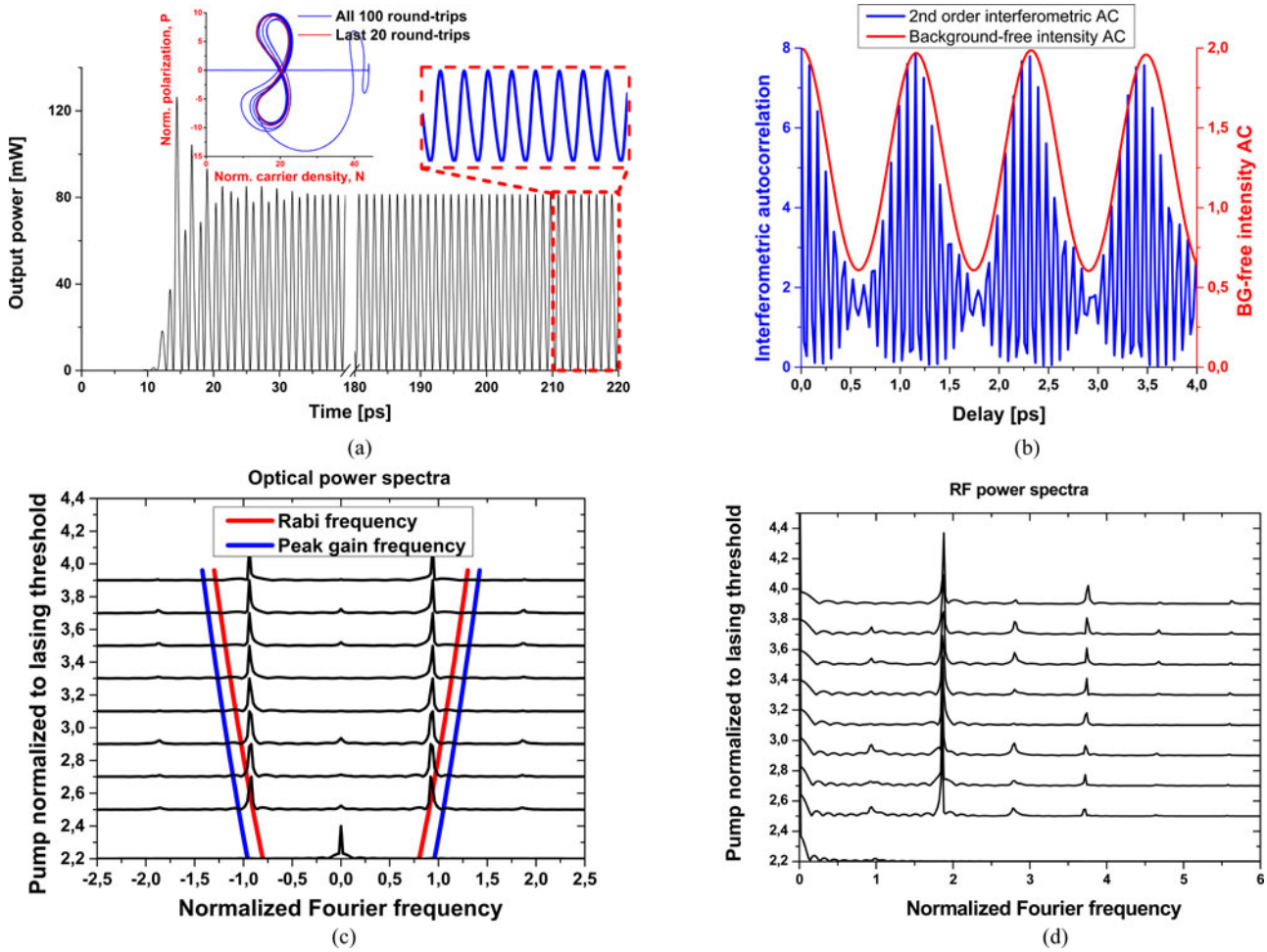

Fig. 6. Results of numerical simulations with TW model for QCL with the cavity length of 100 μm: (a) Waveform: zoom- in at the end of the simulation domain shows regular self-pulsations with sub-picosecond pulse width. Inset shows P-N attractor. (b) AC traces. In (a) and (b) p = 2.5 (above the RNGH threshold). (c) Evolution of the optical spectrum with the pump rate. (d) RF power spectra which shows the main harmonic at about twice of the cold cavity mode spacing.

blue curve] as well as in the regime of regular RNGH self-pulsations [inset in Fig. 6(a) red curve]. This behavior indicates an "off-diagonal long range order" in the system, as predicted by Graham and Haken [7]. Note that a similar behavior is also predicted for Dicke superradiance (SR) [34], [20]. The similarity is even far more striking: The master equation for RNGH instability behavior can be put in the form that bears a closed formal analogy to the description of condensation phenomena, such as superconductivity [7]. But in [20] (and also in [35]), the SR emission is also shown to be governed by the master equation in the form of Ginzburg-Landau equation. Continuing these parallels we note that in the pioneering work of Risken and Nummedal [6], the approximate analytic solution for the regime of RNGH self-pulsations was obtained when the optical filed is entirely defined by the medium polarization, so as $E \propto P$. The same relationship between E and P applies to the case of Dicke superradiance [20], [35]. There is however one important difference between the two regimes. The RNGH instability is usually analyzed in a CW operating laser when the active medium is under continuous wave pumping. The SR pulse emission occurs from a strongly pumped active medium, when the initial optical field is close to zero. In practice this is achieved with pumping by short and intense optical or electrical pulses [34], [36]–[40]. Taking all these considerations into account, we attribute the first emission burst in Figs. 6(a) to SR. See also discussion in [33].

Next, it was shown that SR in short samples is different from the cooperative emission in long samples [20], [35], [41]. The borderline between the two cases is set by the coherence length of the SR emission (SR pulse width). In case of long samples, the situation is such that sample domains of the size of the coherence length emit independently of each other. The output pulse is the result of incoherent superposition of SR emission from different sample domains. As a result, the overall pulse width broadens and its amplitude decreases.

In a similar way, we may conjecture that regular RNGH self-pulsations occur when QCL cavity is shorter than coherence length. Otherwise, in the case of a long QCL sample, different sample domains are mutually incoherent with respect to emission into unstable cavity modes and compete with each other at the initial stage. As a result, an erratic pattern of the field is established in the cavity at a later stage. As seen in Fig. 4, the

optical field pattern almost repeats itself on subsequent round-trips in the cavity, however the coherence length remains much shorter than the cavity length. The coherence time measured from the interferometric AC trace in Fig. 3(b) as a half-width at half maximum (HWHM) of the central lobe above the background is about 2 ps, which corresponds to the duration of the transients in Fig. 3(a) (and Fig. 4(a)). The coherence length is thus about 180μm which is very short compare to millimeter cavity length. On the other hand, in short-cavity QCLs, the coherence time is comparable to a single pass through the sample. The interferometric AC traces in Figs. 3(b) and 6(b) provide an evidence for this keystone difference.

E. The Role of Carrier Diffusion, Carrier Population and Coherence Gratings

In Fig. 7(a) we study the effect of coherence grating on the gain spectrum (increment) for multimode instability by examining the highest gain frequency $\Omega_{\max}$ in the solution of (15) as a function of the pump rate p. These numerical studies complement and confirm the outcomes of our analytical studies from [26].

As a reference, we show the frequency $\Omega_{\max}$ obtained by numerically solving the eigen problem (15) with QCL parameters from Table I and coherence grating relaxation time $T_{2\_g} \neq 0$ (solid blue curve) as well as the calculated Rabi frequency (17) (dashed blue curve) under the same operation conditions. These two reference curves are thus obtained in the presence of mode coupling via scattering on the coherence grating in addition to the coupling via carrier population grating.

The effect of coherence grating can be excluded from (15) by considering the limit $T_{2\_g} \to 0$. We achieve this via reducing T_{2_g} by a factor of 10^{11} while simultaneously maintaining (i) the average decoherence rate ($T_{2\_\mathrm{eff}} \neq 0$) and (ii) the mode coupling via SHB-induced grating of the carrier distribution ($T_g \neq 0$). This represents very well the limit of $T_{2\_g} \to 0$, when there is no mode coupling via scattering on the coherence grating. We find that the system (15) still reveals instability and this instability is caused by the SHB effect only. For the pump rates up to p $\sim$ 10, the spectral shape of the instability increment Re(Λ) is similar to the one depicted in Fig. 1(b). Thus the instability gain spectra do not indicate a change in the mechanism of multimode instability. In Fig. 7(a) we add the superscript "(SHB)" in order to distinguish this case and plot the frequency $\Omega_{\max}^{(\mathrm{SHB})}$ calculated numerically from (15) and $\Omega_{\mathrm{Rabi}}^{(\mathrm{SHB})}$ from (17) for the case when T_{2_g} is reduced by a factor of 10^{11} (solid and dashed red curves, respectively).

In [9], Gordon *et al.*, the expression (18) was obtained for the maximum frequency of the multimode instability increment caused by the SHB effect, that is in the case we have just discussed above. In Fig. 7(a) we indicate this frequency as $\Omega_{\mathrm{SHB}}^{[9]}$ and plot it (green curve) as a function of the pump rate using the parameters of QCL from Table I.

The following conclusions can be drawn from comparison between different curves in Fig. 7(a):

i) In the presence of coherence grating ($T_{2\_g} \neq 0$), the highest gain frequency $\Omega_{\max}$ is very close to the Rabi frequency Ω_{Rabi}. Like the last one, $\Omega_{\max}^2$ exhibits a linear growth with the pump rate p (solid blue curve in Fig. 7(a)). This behavior is a signature of a multimode RNGH-like instability (see Section I).

ii) Without coherence grating ($T_{2\_g} \to 0$), both frequencies reduce to $\Omega_{\max}^{(\mathrm{SHB})}$ and $\Omega_{\mathrm{Rabi}}^{(\mathrm{SHB})}$, respectively (solid and dashed red curves), and $[\Omega_{\max}^{(\mathrm{SHB})}]^2$ does not follow the linear growth of $[\Omega_{\mathrm{Rabi}}^{(\mathrm{SHB})}]^2$ anymore. However even at the pump rate as high as p = 5 times above the lasing threshold, $\Omega_{\max}^{(\mathrm{SHB})}$ is only by a factor of 1.1 lower than $\Omega_{\mathrm{Rabi}}^{(\mathrm{SHB})}$. Therefore, we cannot attribute it to a markedly different behavior than the one observed in the presence of additional mode scattering on the coherence grating. Inclusion of the coherence grating just slightly increases the highest instability frequency in the 4×4 submatrix in (15).

iii) The frequency $\Omega_{\mathrm{SHB}}^{[9]}$ [(18)] obtained in [9], Gordon *et al.*, for the case without coherence grating, that is for case we discussed in (ii), is significantly lower than the Rabi flopping frequency $\Omega_{\mathrm{Rabi}}^{(\mathrm{SHB})}$ (and our frequency $\Omega_{\max}^{(\mathrm{SHB})}$). As a consequence it was attributed in [9] to a multimode instability of a different kind. In fact, as we discussed in Appendix A, the original system of the coupled mode equations in Gordon *et al.* contains a set of omissions, leading to a mistake that $\Omega_{\mathrm{SHB}}^{[9]} << \Omega_{\mathrm{Rabi}}^{(\mathrm{SHB})}$.

The coherence grating has a much stronger impact on the eigen solutions of the 5×5 block in (15). In Fig. 7(b) we plot the spectra of the Lyapunov exponents with the largest real parts in the 4×4 (red curves) and 5×5 (blue curves) blocks of (15) for the pump rate p = 10. Once again we compare cases when the coherence grating is present ($T_{2\_g} \neq 0$, solid curves) and when it is absent ($T_{2\_g} \to 0$, dashed curves). We observe that without coherence grating (when $T_{2\_g} \to 0$) the increment of instability in the 4×4 matrix block (red curves) increases and its spectrum shifts to lower frequencies, in accordance with Fig. 7(a). The behavior of the instability increment in the 5×5 block has much in common with the 4×4 block but the increment values are shifted in Fig. 7(b) toward negative Lyaponov exponents. Only without coherence grating ($T_{2\_g} \to 0$), the increment reaches positive values and RNGH instability occurs at p = 10 (see dashed blue curve in the inset of Fig. 7(b)). Note that RNGH instability does not occur at p = 9 because $T_{2\_\mathrm{eff}}/T_1 \neq 0$ [6]. Once the coherence grating is present ($T_{2\_g} \neq 0$), the RNGH instability threshold in 5×5 matrix block increases by several times, to around p = 60 (see Fig. 1(a)). In this way it remains only one pleasurable explanation for the low self-pulsations threshold observed in experiments with QCLs. Namely we conclude that it is related with the instability arising from the 4×4 matrix block in (15) due to a combined effect of the carrier population and carrier coherence gratings.

The carrier diffusion causes relaxation of the induced gratings with the relaxation rates $\propto D/\lambda^2$. In our recent study [33] we have elucidated the role of the carrier diffusion in QCLs and LDs by considering various emission wavelengths. We have shown that in all considered cases of QCLs, the carrier diffusion

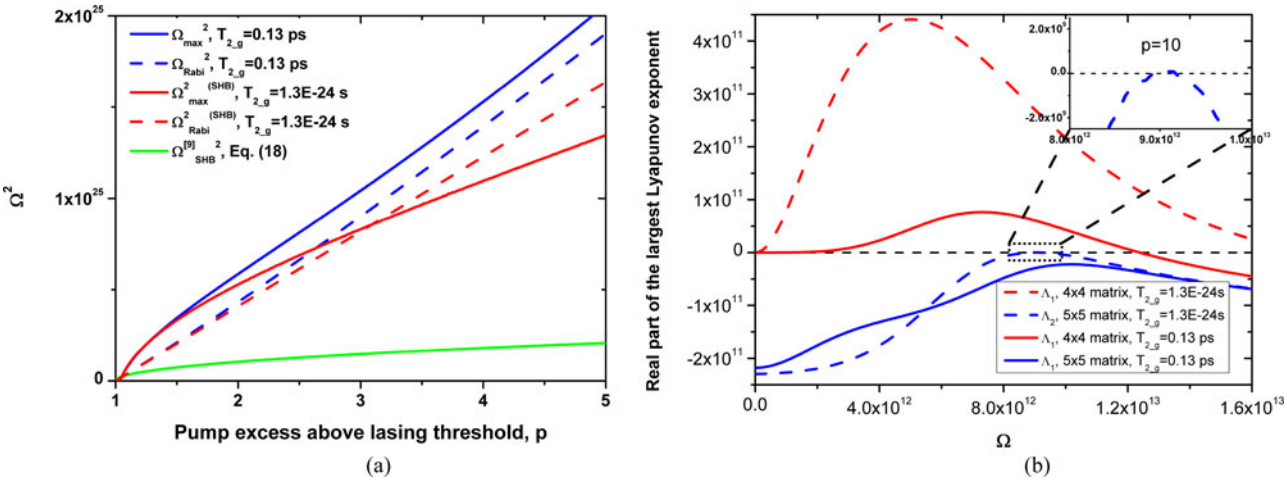

Fig. 7. (a) We plot the squares of the following frequencies as a function of the pump rate, using parameters of QCL from Table I ($T_g = 0.927$ ps, $T_{2\_\mathrm{eff}} = 0.14$ ps and $T_{2\_g} = 0.13$ ps unless stated otherwise): the highest instability gain frequency $\Omega_{\max}$ calculated numerically from the eigen problem of (15) ($T_{2\_g} \neq 0$, solid blue curve) and corresponding Rabi oscillations frequency (17) (dashed blue curve); the frequency $\Omega_{\max}^{(\mathrm{SHB})}$ (solid red curve) and the Rabi frequency $\Omega_{\mathrm{Rabi}}^{(\mathrm{SHB})}$ (dashed red curve) obtained without coherence grating (T_{2_g} is reduced by a factor of 10^{11}); and finally the frequency $\Omega_{\mathrm{SHB}}^{[9]}$ calculated from (18) (green curve). (b) Spectra of instability increments (largest real parts of the Lyapunov exponents) of the two matrix blocks of 4×4 (red curves) and 5×5 (blue curves) sizes for QCL with parameters from Table I. The pump rate excess above threshold is $p = 10$. The solid curves stand for the case considered in this paper when we include the coherence grating effects ($T_{2\_g} = 0.13$ ps), while the dashed curves represent the case when the coherence grating relaxation time T_{2_g} is reduced by a factor of 10^{11}, suppressing all effects caused by the coherence grating. The insets show zooms to the highest RNGH instability increments in the 5×5 matrix block when $T_{2\_g} \to 0$ (no coherence grating effects).

does not raise the RNGH threshold to prohibitively high levels. The implication of the carrier diffusion effect is totally different in the case of QW laser diodes operating in the VIS or NIR spectral range [33]. Even though the ambipolar diffusion in the QWs of these devices is much weaker than the diffusion of electrons in QCLs (see Table I in [33]), the relaxation due to diffusion is more perceptible because of the shorter wavelength and periods of induced gratings. As a consequence, the second threshold values predicted from the linear stability analysis are of several hundred times above the lasing threshold. Indeed, it is commonly acknowledged that QW laser diodes with monolithic FP cavities do not show RNGH instabilities in the range of pump currents that can be reached in practice. At practical pump rates, which are all below the RNGH threshold, FP LDs with uniform QWs show an ordinary behavior of a Class-B laser, which is characterized by excitation of damped relaxation oscillations followed by a transition to CW lasing regime.

In Fig. 8 we show the output waveform and P-N attractor simulated numerically with our TW model for a 100 μm long single-section GaN LD pumped above the RNGH threshold, at p = 400. At such high pump rate, LD exhibits behavior which is similar to QCLs biased at above the RNGH instability threshold. The output waveform reveals the SR emission burst followed by regular RNGH self-pulsations [compare with Fig. 6(a)].

Note that during the SR emission burst, the order parameter is large and approaches a half of the initial carrier density stored in the system.

We thus conclude that VIS-NIR range QW LDs have very high RNGH self-pulsations threshold because of rapid relaxation of the carrier coherence and population gratings. Whereas the RNGH instability threshold in single-section QW LDs is not reachable under realistic experimental settings, there are several

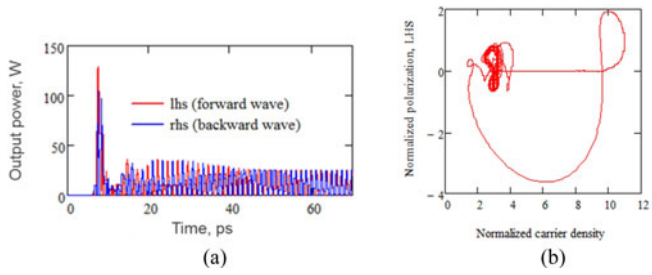

Fig. 8. Results of numerical simulations with TW model for GaN LD with the cavity length of 100 μm: Waveform (a) and P-N attractor (b). The red (blue) trace corresponds to the wave propagating in the forward (backward) direction. The active region contains 3×3 nm InGaN QWs, ridge waveguide width is 2 um and material gain parameters can be found in Ref. [20]. The ambipolar diffusion coefficient in QWs is of D = 7 cm^2/s [33].

considerations that indirectly support our conclusion. Reaching the SR emission in short-length mesa-etched structures comprising GaAs QWs was attempted in [42] under short-pulse optical pumping. However no evidence of SR emission was observed. We may attribute this to the fact that threshold condition for RNGH instability has not been reached in these experiments as the pump rate was too low.

Lowering the RNGH instability threshold (and reaching SR emission) in a single-section LD can be achieved by reducing the contribution of diffusion to the relaxation rates of the carrier coherence and population gratings. This bring us to the insight that low-dimensional semiconductor heterostructures such as quantum dots (QDs) or quantum dashes (QDash) can be used as active gain material in order to avoid prohibitively high RNGH threshold. Surprisingly, in [43], starting from totally different considerations, a similar conclusion was made about

semiconductor heterostructures suitable for SR emission. Thus according to [43], SR emission is not possible with the active gain medium utilizing bulk semiconductor material or uniform QW heterostructures. One needs to use QDs or to introduce an additional quantization degree in QWs by applying strong magnetic field. The SR emission from magneto-excitons in InGaAs/GaAs QW was confirmed in [36] under short-pulse optical pumping.

There is another way to reduce the RNGH threshold in a semiconductor laser. It consists in incorporating a saturable absorber [9], [10] (see also Introduction and Section II-C). Technically this is achieved by implementing several separately contacted sections in the monolithic cavity of LD. The cavity sections which are positively biased provide the optical gain while a negatively biased section behaves as a saturable electroabsorber. Under moderate negative biases applied to the absorber section, the laser exhibits passive mode-locking or Q-switching operation. However with further increasing negative bias, yielding shorter recovery time and larger absorption coefficient, a different emission regime occurs. At threshold of Q-switched lasing operation and under pulsed current pumping, the laser reveals features of SR-like emission. These features have been experimentally observed in multi-section GaAs, AlGaInAs and GaN QW lasers [37]–[40]. Unfortunately all experimental studies reported in the literature do not distinguish the first emission burst from the subsequent self-pulsations, which can be modulated with a Q-switching pulse envelope. Nevertheless a clear Rabi splitting was observed in the optical spectrum of such multi-section LDs when these were expected to produce SR emission [37]. So far there were no detailed reports on experimental studies on RNGH instability in multi-section laser diodes, and we believe that this subject will receive further attention in future.

IV. Conclusion

We have clarified conditions for multimode RNGH instability in a Fabry-Pérot cavity laser and shown that low instability threshold observed in QCLs is due to a combined effect of the carrier coherence and carrier population gratings. We have studied the impact of the cavity length on the waveform of RNGH self-pulsations and shown that a short-cavity QCL can produce regular train of ultrashort pulses. Our findings open up a novel practical way to achieve ultra-short pulse production regimes in QCLs operating in the mid-infrared spectral range.

Appendix A
Adiabatic Approximation Test

In this supplementary section we consider adiabatic-following approximation that applies to *bidirectional ring lasers* operating on two counter-propagating waves or single-mode *FP cavity lasers.* In these lasers, the standing wave pattern of the field in the cavity leads to the spatial hole burning in the distribution of population inversion. Respectively, our considerations presented below do not apply for a single-frequency *unidirectional ring laser* from [6], [7].

The adiabatic-following approximation for the medium polarization is valid when polarization dynamics is slow and follows instantaneously the optical field in the cavity [8]. For solid state lasers, including semiconductor LDs and QCLs, the dephasing time T_2 is much smaller than the relaxation T_1. Therefore under adiabatic-following approximation, the behavior of these systems falls into Class-B laser dynamics. These dynamical systems are very well studied, including the cases with mode coupling due to back-scattering and induced population grating. One example can be found in a review [22].

In order to obtain such approximation for our coupled-mode system (7)–(10), we set the time derivatives in (8) and (9) to zero, yielding the following instantaneous polarization harmonics:

$$\eta_{\pm} = \frac{i\mu}{2\hbar}\left(E_{\pm}\Delta_0 + E_{\mp}\Delta_2^{\mp}\right)T_2 \tag{19}$$

$$\eta_{\pm\pm} = \frac{i\mu}{2\hbar}\left(E_{\pm}\Delta_{\mp}\right)T_{2\_g} \tag{20}$$

where for the purpose of this test we have excluded the diffusion terms, assuming that $T_{2\_\mathrm{eff}} = T_{2\_g} = T_2$, and $T_g = T_1$. Substituting these in (7), (9) and (10), we find that

$$\frac{n_g}{c}\frac{\partial E_{\pm}}{\partial t} = \mp\frac{\partial E_{\pm}}{\partial z} + \frac{NT_{2\_\mathrm{eff}}\mu^2\Gamma\omega}{2c\hbar n\varepsilon_0}\left(E_{\pm}\Delta_0 + E_{\mp}\Delta_2^{\mp}\right) - \frac{1}{2}l_0E_{\pm} \tag{21}$$

$$\frac{\partial(\Delta_0 + \Delta_2^{+}e^{2ikz} + \Delta_2^{-}e^{-2ikz})}{\partial t} = \frac{\Delta_{pump}}{T_1} - \frac{\Delta_0 + \Delta_2^{+}e^{2ikz} + \Delta_2^{-}e^{-2ikz}}{T_1} \times \left[1 + a\left((E_{-}^{*}E_{-} + E_{+}^{*}E_{+}) + 2Re(E_{-}^{*}E_{+}e^{-2ikz})\right)\right] \tag{22}$$

where we have introduced the saturation parameter $a = T_1T_2\mu^2/\hbar^2$. This system of equations is in perfect agreement with the well-known Class-B laser model (e.g., see (1.10) and (1.11) in [22]). In contrast to our coupled-mode expansion, the adiabatic approximation that follows from the (8)–(10) in [9] disagrees with this well-established model for a Class-B laser.

Appendix B
Experimental Observations of RNGH Instability

The experimental data available in the literature attest that RNGH instability does not always lead to observation of a clear Rabi splitting in the optical mode spectrum of a QCL. In some experimental realizations, RNGH instability causes just a broadening of the lasing spectrum to the offset frequencies of the order of the Rabi oscillation frequency. Indeed, the appearance of Rabi splitting in the optical spectrum can be tailored by changing the sample temperature [5], [9], [15]. For example, in [9] at low temperatures (80-150 K) the measured lasing spectra in a buried heterostructure QCL sample are just simply broadened, but with increasing temperature, the Rabi splitting between mode clusters becomes more apparent. At room temperature conditions, two distinct mode clusters emerge in the optical spectrum. Because temperature dependence of carrier

diffusion has been found to produce a too weak contrast change in the SHB grating [9], the thermal population of injector levels yielding temperature-dependent saturable absorption has been suggested as one of the possible mechanisms. However in [15], QCL samples show totally opposite spectral behavior with the temperature. The optical spectra reveal lasing mode clusters with separation of $\sim$20–30 cm^{-1} at liquid He temperature (6 K) while at an increased temperature of 77 K, no clear spectral splitting is observed in the broad multimode emission spectrum. Although available experimental reports do not elucidate the nature of the temperature effect, most importantly they allows us to spot one common feature: Once a laser sample exhibit clear Rabi splitting at some temperature, it also reveals very broad multimode emission at other temperatures, which can be with or without mode clustering. The overall spectral width of such multimode emission practically does not change with the temperature, reaching $\sim$35-40 cm^{-1} at the pump rate of p $\sim$ 1.7-1.8 times above lasing threshold and the width of $\sim$60 cm^{-1} for p $\sim$ 3.5-3.6. Therefore we conclude that the multimode dynamics responsible for such large spectral broadening at different temperatures is governed by the same processes. Hence an observation of large spectral broadening on the order of Ω_{Rabi} already provides an indication of multimode RNGH instability, whilst the optical spectrum might not be split in two distinct mode clusters. This conclusion is in agreement with experimentally measured QCL spectra in [11].

Even if the two distinct mode clusters appear in the lasing spectrum, their frequency spitting is not necessary equal to 2 Ω_{Rabi}. The pump rate dependence of the Rabi frequency [see (17)] assumes that this splitting is proportional to the square root of the output power. In [5], [9], this behavior is confirmed for the range of QCL output power up to 36 mW and the frequency splitting up to 1 THz is observed in 3 μm-wide buried heterostructure lasers. However for 10-15 μm wide ridge waveguide lasers from [9] and [15], the spectral splitting is clamped at about 0.8 THz for the output power of $\sim$25 mW and higher. This is not surprising because the notion of the Rabi splitting in the gain spectrum of a laser is introduced considering small-amplitude perturbations to the initial optical field in the cavity. This small-signal picture is very different from the situation in the laser undergoing large-amplitude self-pulsations. At high pump rates, the overall spectral broadening due to multimode RNGH instability can be smaller than 2 Ω_{Rabi}.

In the cited works, the complex structure of the lasing transition in QCL is usually not taken into account in the interpretation of experimental results. At the same time inhomogeneous features in the optical gain curve or dispersive characteristics of the cavity (e.g., due to backscattering from microcracks [44]) may significantly reshape the spectral envelop of multimode RNGH emission.

All experimental studies cited here are limited to long-cavity QCL samples of 1.5–4 mm length. The data reported in [15] might lead to a conjecture that sample length has an impact on the appearance of the two distinct mode clusters. Unfortunately no detailed experimental study on the effect of the sample length on RNGH instability has been reported.

ACKNOWLEDGMENT

D. L. Boiko is grateful to Vladimir Kocharovsky and Ekaterina Kocharovskaya for valuable discussions.

REFERENCES

[1] J. Faist, *Quantum Cascade Lasers*, 1st ed. London, U.K.: Oxford Univ. Press, 2013.
[2] H. A. Haus, "Mode-locking of lasers," *IEEE J. Sel. Topics Quantum Electron.*,vol. 6, no. 6, pp. 1173–1185, Nov./Dec.2000.
[3] R. Paiella *et al.*, "High-speed operation of gain-switched midinfrared quantum cascade lasers," *Appl. Phys. Lett.*, vol. 75, no. 17, pp. 2536–2538, 1999.
[4] C. Y. Wang *et al.*, "Mode-locked pulses from mid-infrared quantum cascade lasers," *Opt. Express*, vol. 17, pp. 12929–12943, 2009.
[5] C. Y. Wang *et al.*, "Coherent instabilities in a semiconductor laser with fast gain recovery," *Phys Rev A*, vol. 75, 2007,Art. no. 031802(R).
[6] H. Risken and K. Nummedal, "Self-pulsing in lasers," *J. Appl. Phys.*, vol. 39, pp. 4662–4672, 1968.
[7] R. Graham and H. Haken, "Quantum theory of light propagation in a fluctuating laser-active medium," *Z. Phys*,. vol. 213, pp. 420–450, 1968.
[8] M. D. Crisp, "Adiabatic-following approximation," *Phys. Rev. A*, vol. 8, pp. 2128–2135, 1973.
[9] A. Gordon *et al.*, "Multimode regimes in quantum cascade lasers: From coherent instabilities to spatial hole burning," *Phys. Rev. A*, vol. 77, no. 5, 2008, Art. no. 053804.
[10] H. Knapp, H. Risken, and H. D. Vollmer, "Instability of laser CW oscillations in the presence of a passive medium," *Appl. Phys.*, vol. 15, pp. 265–270, 1978.
[11] T. S. Mansuripur *et al.*, "Single-mode instability in standing-wave lasers: The quantum cascade laser as a self-pumped parametric oscillator," *Phys. Rev. A*, vol. 94, 2016, Art. no, 063807.
[12] I. Grave, M. Segev, and A. Yariv, "Observation of phase conjugation at 10.6 pm via intersubband third-order nonlinearities in a GaAs/AIGaAs multi-quantum-well structure," *Appl. Phys Lett*, vol. 60, 1992, Art. no. 2717.
[13] F. Capasso, C. Sirtori, and A. Y. Cho, "Coupled quantum well semiconductors with giant electric field tunable nonlinear optical properties in the infrared," *IEEE J. Quantum Electron.*, vol. 30, no. 5, pp. 1313–1326, May 1994.
[14] T. Herr *et al.*, "Temporal solitons in optical microresonators," *Nature Photonics*, vol. 8, no. 2, pp. 145–152, 2014.
[15] M. Bugajski, K. Pierściński, D. Pierścińska, A. Szerling, and K. Kosiel, "Multimode instabilities in mid-infrared quantum cascade lasers," *Photonics Lett. Poland*, vol. 5, no. 3, pp. 85–87, 2013.
[16] Vl. V. Kocharovsky, A. A. Belyanin, E. R. Kocharovskaya, and V. V. Kocharovsky "Superradiant lasing and collective dynamics of active centers with polarization lifetime exceeding photon lifetime," in *Adv. Lasers*, O. Shulika and I. Sukhoivanov, Eds. New York, NY, USA: Springer-Verlag, 2015, pp. 49–69.
[17] J. Ohtsubo, *Semiconductor Lasers, Stability, Instability and Chaos*, 3rd ed. New York, NY, USA: Springer-Verlag, 2013.
[18] R H Pantell and H E Puthoff, *Fundamentals of Quantum Electronics*. Hoboken, NJ, USA: Willey, 1969.
[19] S. Appelt *et al.*, "Theory of spin-exchange optical pumping of 3He and 129Xe," *Phys. Rev. A*, vol. 58, pp. 1412–1439, 1998.
[20] D. L. Boiko and P. P. Vasil'ev, "Superradiance dynamics in semiconductor laser diode structures," *Opt. Express*, vol. 20, pp. 9501–9515, 2012.
[21] L. A. Lugiato *et al.*, "Multimode instabilities in a homogeneously broadened ring laser," *Phys Rev. A*, vol. 32, pp. 1563–1575, 1985.
[22] N. V. Kravtsov, E. G. Lariontsev, and A. N. Shelaev, "Oscillation regimes of ring solid-state lasers and possibilities for their stabilization," *Laser Phys.*, vol. 3, pp. 21–62, 1993.
[23] F. Prati and L. Columbo, "Long-wavelength instability in broad-area semiconductor lasers," *Phys. Rev. A*, vol. 75, 2007, Art. no. 053811.
[24] L. Gil and G. Lippi, "Phase instability in semiconductor lasers," *Phys. Rev. Lett.*, vol. 113, 2014, Art. no. 213902.
[25] C. Serrat and C. Masoller, "Modeling spatial effects in multilongitudinal-mode semiconductor lasers," *Phys. Rev. A*, vol. 73, 2006, Art. no. 043812.
[26] N. Vukovic, J. Radovanovic, V. Milanovic, and D. L. Boiko, "Analytical expression for Risken-Nummedal-Graham-Haken instability threshold in quantum cascade lasers," *Opt. Express*, vol. 24, pp. 26911–26929, 2016.

[27] E. Roldan, G. J. de Valcarcel, F. Prati, F. Mitschke, and T. Voigt, "Multilongitudinal mode emission in ring cavity class B lasers," 2004. [Online]. Available: http://arxiv.org/abs/physics/0412071v1
[28] S. L. McCall and E. L. Hahn, "Self-induced transparency," *Phys. Rev.*, vol. 183, pp. 457–485, 1969.
[29] E. N. Lorenz, "Deterministic non periodic flow," *J. Atmos. Sci.*, vol. 20, pp. 130–141, 1963.
[30] A. K. Wojcik *et al.*, "Generation of picosecond pulses and frequency combs in actively mode locked external ring cavity quantum cascade lasers," *Appl. Phys. Lett.*, vol. 103, 2013, Art. no. 231102.
[31] Y. Wang and A. Belyanin, "Active mode-locking of mid-infrared quantum cascade lasers with short gain recovery time," *Opt. Express*, vol. 23, pp. 4173–4185, 2015.
[32] J.-C. Diels and W. Rudolph, *Ultrashort Laser Pulse Phenomena*, 2nd ed. New York, NY, USA: Academic, 2006, p. 463.
[33] N. Vukovic, J. Radovanovic, V. Milanovic, and D. Boiko, "Multimode RNGH instabilities of Fabry-Pérot cavity QCLs: Impact of diffusion," *Opt. Quantum Electron.*, vol. 48, pp. 1–10, 2016.
[34] R. H. Dicke, "Coherence in spontaneous radiation processes," *Phys. Rev.*, vol. 93, pp. 99–110, 1954.
[35] D. L. Boiko and P. P. Valsil'ev, "Longitudinal polariton condensation and superradiant emission in semiconductor edge-emitting laser structures," 2011. [Online]. Available: https://arxiv.org/abs/1112.1298
[36] G. T. Noe, II *et al.*, "Giant superfluorescent bursts from a semiconductor magneto-plasma," *Nat. Phys.*, vol. 8, pp. 219–224, 2012.
[37] P. P. Vasil'ev, "Femtosecond superradiant emission in inorganic semiconductors," *Rep. Prog. Phys.*, vol. 72, 2009, Art. no. 076501.
[38] M. Xia, R. V. Penty, I. H. White, and P. P. Vasil'ev, "Femtosecond superradiant emission in AlGaInAs quantum-well semiconductor laser structures," *Opt. Express*, vol. 20, pp. 8755–8760, 2012.
[39] V. F. Olle, P. P. Vasil'ev, A. Wonfor, R. V. Penty, and I. H. White, "Ultrashort superradiant pulse generation from a GaN/InGaN heterostructure," *Opt. Express*, vol. 20, pp. 7035–7039, 2012.
[40] D. L. Boiko *et al.*, "Superfluorescent emission in electrically pumped semiconductor laser," 2013. [Online]. Available: https://arxiv.org/abs/1302.0263
[41] F. T. Arecchi and E. Courtens, "Cooperative phenomena in resonant electromagnetic propagation," *Phys. Rev. A*, vol. 2, pp. 1730–1737, 1970.
[42] L. Kappei, "Dynamics and coherent effects of high density plasmas in semiconductor nanostructures," Ph.D. dissertation, EPFL, Inst. of Quantum Electron. & Photonics, Swiss Fed. Inst. of Technol., Lausanne, Switzerland, 2005.
[43] A. A. Belyanin, V. V. Kocharovskii, and Vl. V. Kocharovskii, "Recombination superradiance in semiconductors," *Laser Physics*, vol. 2, pp. 952–964, 1992.
[44] X. Zeng and D. L. Boiko, "1/f noise in external-cavity InGaN diode laser at 420 nm wavelength for atomic spectroscopy," *Opt. Lett.*, vol. 39, vol. 6, pp. 1685–1688, 2014.

Nikola N. Vuković was born in Belgrade, Serbia, in 1989. He received the B.Sc. and the M.Sc. degrees in electrical engineering in 2012 and 2013, respectively, from the School of Electrical Engineering, University of Belgrade, Belgrade, Serbia, where he is currently working toward the Ph.D. degree. His research interest includes the design and optimization of semiconductor quantum nanostructures, metamaterials, and ultrafast nonlinear optics.

Jelena Radovanović was born in Belgrade, Serbia, in 1973. She received the B.Sc. degree (five years program) in 1997, the M.Sc. degree (two years program) in 1999, and the Ph.D. degree in 2001, all in electrical engineering, from the School of Electrical Engineering, University of Belgrade, Belgrade Serbia, where she is currently employed as a Full Professor.

She has coauthored 87 articles in refereed international journals, more than 100 conference papers presented at international and national conferences, including several invited lectures, two monographs, one book chapter, and two university textbooks. Her research interests include optical properties of semiconductor nanostructures, modelling of quantum cascade lasers and semiconductor-based metamaterials, as well as photonic heterostructures. She is one of the founders and currently a President-Elect of the Optical Society of Serbia.

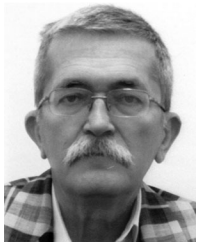

Vitomir Milanović was born in Jagodina, Serbia, in 1947. He received the B.Sc. EE degree in 1971, M.Sc. EE degree in 1977, and the Ph.D. degree in 1983, all from the School of Electrical Engineering in Belgrade, University of Belgrade, Belgrade, Serbia, where he was employed as a Full Professor until 2012. Since 2013 he has been a Professor Emeritus. His past and current teaching activities include several courses at undergraduate, former graduate, and Ph.D. level.

He has coauthored three university textbooks, a book on selected problems in solid state physical electronics, one monograph, and a chapter in an international monograph. So far, he has published 193 papers in international journals. His research interests include physical electronics and solid state physics. The majority of his works have been focused on studying quantum effects in semiconductor nanostructures. In the last few years, his scientific activity is dedicated to modern topics related to quantum cascade lasers and analysis of tunneling times in nanostructures and photonic crystals.

In 1990, he received an award of the School of Electrical Engineering for the endowment of Prof. Branko Raković and in 1991, the October Award of the city of Belgrade. He is the member of the Serbian Scientific Society.

Dmitri L. Boiko received the Diploma (Hons.) in applied mathematics and physics and the M.Sc. degree (Hons.) in laser physics from the Moscow Institute of Physics and Technology (MIPT), Dolgoprudny, Russia, in 1993. In 1998, he received the Ph.D. degree from the MIPT and Research & Development Institute "Polyus" in Moscow, Russia. He has been working on dynamics of solid state ring lasers, multisession semiconductor edge emitting lasers, vertical cavity surface emitting lasers, as well as phase coupled laser arrays. His career path propagates via Ecole Nationale Supérieure de Sciences Appliquées et de Technologie, Lannion, France, and Ecole Polytechnique Fédérale de Lausanne, Lausanne, Switzerland. Since 2009, he is with the Center Suisse d'Electronique et de Microtechnique, Neuchatel, Switzerland, holding the position of Expert. His current research activities are focused on the atomic clocks and gyroscopes, as well as ultrafast lasers.